Heribert Kopeinik, BSc

Organic Diodes and Photovoltaic Cells based on Conductive Cellulose Fiber Networks

MASTER THESIS

For obtaining the academic degree
Diplom-Ingenieur

Master Programme of
Technical Physics

Graz University of Technology

Supervisor:

Dipl.-Phys. Dr.rer.nat. Bettina Friedel

Co-Supervisor:

Univ.-Prof. Ph.D Peter Hadley

Institute of Solid State Physics

Graz, November 2014

"*There is a theory which states that if ever anyone discovers exactly what the Universe is for and why it is here, it will instantly disappear and be replaced by something even more bizarre and inexplicable.*
There is another theory which states that this has already happened."

Douglas Adams, The Restaurant at the End of the Universe

Acknowledgements

I would like to express my special appreciation and thanks to my supervisor Dipl.-Phys. Dr.rer.nat. Bettina Friedel, whose support, ideas and positive criticism led me through the development of this thesis. Furthermore, I am grateful to Ao.Univ.-Prof. Mag. Dr.rer.nat Robert Schennach and Univ.-Prof. Ph.D. Peter Hadley for their advice and assistance. It is a pleasure to thank my colleagues and friends at the Solid State Institute for hours of fruitful discussions during office hours and coffee breaks.

Furthermore, I am thankful to Graz University of Technology and the NAWI-Graz for the TU F-NW4-UHLIG1 scholarship that advanced my research and allowed me to participate at the Gordon Research Conference.

Finally, I would like to gratefully mention my family and all my close friends, who encouraged and supported me throughout my studies.

Abstract

Being natural and biologically degradable are two qualities required for materials in modern organic optoelectronics, which are both combined in natural wood cellulose fibers. Their advantages are their mechanical flexibility and cellulose's good optical transparency, while being cheap and abundant. On the downside, they possess a relatively rough surface, which is a challenging property when combined with thin film applications/architectures. Additionally, they are electrical insulators which is also not desired for an electrode.

In this thesis a simple way to fabricate electrically conductive cellulose fiber networks, suitable as semitransparent conductive substrate in organic solar cells, is shown. Therefore, approaches with reduced graphene oxide and long silver nanowires were made to provide the electrical conductivity. For deposition, simple drop-casting and dip-coating procedures were used, respectively. Only the attempts with silver nanowires showed promising sheet resistance down to a few Ohm and were therefore comparable to traditionally used electrodes based on indium tin oxide. The silver nanowires were adsorbed to the cellulose fibers by a dip-coating process, forming networks around and between them. PEDOT:PSS was used to glaze the surface and as an electron blocking layer.
As proof of concept, organic diodes and organic photovoltaic devices were built, using the fabricated electrically conductive cellulose fiber networks as anode. Thereby P3HT and a blend of P3HT and $PC_{60}BM$ were used as active material for the diodes and the photovoltaic devices, respectively. The devices were finalized with a thermally evaporated aluminum cathode.

To verify the fabricated samples, electrical and optical properties as well as chemical and morphological properties were investigated. Therefore current-voltage characterization, UV/VIS spectroscopy, FTIR spectroscopy, optical microscopy and scanning electron microscopy imaging were performed.

Kurzfassung

Zu den Anforderungen, die an Materialien in modernen optoelektronischen Bauelementen gestellt werden, zählen ihre biologische Abbaubarkeit und Umweltverträglichkeit. Zellulosefasern aus Naturholz erfüllen beide dieser Eigenschaften. Weitere Vorteile der Zellulosefasern sind ihre mechanische Flexibilität sowie ihre gute optische Transparenz. Zusätzlich sind sie billig und in ausreichender Menge vorhanden. Als Nachteil ist ihre raue Oberfläche anzuführen, die in Kombination mit Dünnschichtanwendungen bzw. Dünnschichtarchitekturen eine herausfordernde Eigenschaft darstellt. Zellulose ist ein sehr guter elektrischer Isolator, was als weiteres Manko in der Anwendung als Elektrode von Halbleiterbauelementen zu werten ist.

In dieser Arbeit wird ein einfacher Weg zur Herstellung elektrisch leitfähiger Zellulosefaser-Netzwerke vorgestellt. Diese dienen als leitfähiges, semitransparentes Substrat in organischen Solarzellen. Hierfür wurden Versuche mit reduziertem Graphenoxid (rGO) sowie Silber-Nanodrähte (AgNWs) als elektrisch leitfähiges Additiv durchgeführt. Die leitfähigen Materialien wurden mittels Tauchbeschichtung bzw. mit einem einfachen Auftropfverfahren aufgetragen. Ausschließlich die Versuche mit AgNWs zeigten vielversprechende Resultate mit Flächenwiderständen im zweistelligen Ohm Bereich und waren somit vergleichbar mit den traditionell verwendeten Indium-Zinn-Oxid Elektroden. Die Adsorption der AgNWs an den Zellulosefasern wurde mittels Tauchbeschichtung erreicht. Während diesem Prozess bilden die AgNWs Netzwerke um und zwischen den Zellulosefasern. Zur Überprüfung des Konzeptes, elektrisch leitfähige Zellulosefasern als Anodenmaterial einzusetzen, wurden organische Dioden sowie organische Photovoltaikzellen (OPVs) gefertigt. PEDOT:PSS diente als Lochleitungsschicht sowie zur Verringerung der Oberflächenrauhigkeit. P3HT bzw. eine Mischung aus P3HT und $PC_{60}BM$ wurden als aktives Material für die Dioden bzw. die OPVs verwendet. Als Kathodenmaterial wurde Aluminium auf das Bauteil aufgedampft.

Die hergestellten Proben wurden auf ihre elektrischen, optischen sowie morphologischen und chemischen Eigenschaften hin untersucht. Dazu kamen Strom-Spannungs Charakterisierungen , UV/VIS-Spektroskopie, FTIR-Spektroskopie, optische Mikroskopie sowie Rasterelektronenmikroskopie zur Anwendung.

EIDESSTATTLICHE ERKLÄRUNG

AFFIDAVIT

Ich erkläre an Eides statt, dass ich die vorliegende Arbeit selbstständig verfasst, andere als die angegebenen Quellen/Hilfsmittel nicht benutzt, und die den benutzten Quellen wörtlich und inhaltlich entnommenen Stellen als solche kenntlich gemacht habe. Das in TUGRAZonline hochgeladene Textdokument ist mit der vorliegenden Masterarbeit/Diplomarbeit/Dissertation identisch.

I declare that I have authored this thesis independently, that I have not used other than the declared sources/resources, and that I have explicitly indicated all material which has been quoted either literally or by content from the sources used. The text document uploaded to TUGRAZonline is identical to the present master's thesis/diploma thesis/doctoral dissertation.

Datum / Date	Unterschrift / Signature

Contents

List of abbreviations

η_{Abs}	-	Exciton Generation Efficiency
η_{Coll}	-	Charge Collection Efficiency
η_{ExDiff}	-	Exciton Diffusion Rate
η_{Sep}	-	Charge Separation Efficiency
η	-	Power Conversion Efficiency
A	-	Ampere
AgNW	-	Silver Nanowire
Al	-	Aluminum
AM1.5G	-	Air Mass 1.5 Global
Ar	-	Argon
ATR	-	Attenuated Total Reflection
DBM	-	Dual Beam Microscope
FF	-	Fill Factor
FIB	-	Focus Ion Beam
FTIR	-	Fourier Transformed Infrared
GB	-	Glove Box
GO	-	Graphene Oxide
HOMO	-	Highest Occupied Molecular Orbital
I_{MPP}	-	Maximum Power Point Current
I_{PH}	-	Photo-Current
I_{PHmax}	-	Maximum Photo-Current
I_{SC}	-	Short Circuit Current
I	-	Current
IR	-	Infrared
ITO	-	Indium Tin Oxide
J	-	Current Density
LED	-	Light Emitting Diode

LUMO	-	Lowest unoccupied Molecular Orbital
MPP	-	Maximum Power Point
OD	-	Organic Diode
OPV	-	Organic Photvoltaic
P_{Light}	-	Radiation Density
P_{max}	-	Maximum of Power
P3HT	-	poly(3-hexylthiophene-2,5-diyl)
$PC_{60}BM$	-	phenyl-C61-butyric acid methyl ester
PEDOT:PSS	-	poly(3.4-ethylenedioxythiophene)-poly(styrenesulfonate)
R_{Sub}	-	Electrical Resistance of the Substrate
R	-	Electrical Resistance
rGO	-	Reduced Graphene Oxide
SEM	-	Scanning Electron Microscope
T_{dry}	-	Drying Temperature
t_{dry}	-	Drying Time
T	-	Temperature
t	-	Time
U_{MPP}	-	Maximum Power Point Voltage
U_{OC}	-	Open Circuit Voltage
v_{dip}	-	Dip-In Speed
V_{drop}	-	Volume Dropped
v_{wd}	-	Withdrawal Speed
V	-	Voltage / Volt

1. Introduction

In this introduction the reader will get a quick overview about the motivation of this work. Moreover, it shall offer a chemical and physical basis for further understanding.

1.1. Motivation

Nowadays the call for electronics, based on environmental friendly and flexible materials is omnipresent. Abundant materials, which are biocompatible, biodegradable and of course cheap in production are desired. In several articles and reviews, paper has been declared as a possible candidate as substrate for organic thin film applications [1, 2]. Although the term "paper" has a wide range of appearances, it is traditionally understood as a network of wood pulp fibers. These cellulose fibers typically have a length up to a few millimeters and a diameter of some microns. However, usually its appearance and surface properties are modified to fit its actual purpose. In general, this is accomplished by adding fillers, coatings and/or additives. Although there have been various reports on electrically conductive paper fabricated by infiltration, coating or lamination of the cellulose fiber networks and their application for for electronic devices, the high surface roughness and its wettability is considered as a restrictive factor. Thus the paper is treated chemically or coated with fillers to smooth the surface if used for organic electronic devices.

The scope of this study is to demonstrate the possibility of using cellulose fiber networks for organic thin film diodes. Therefore photoactive organic devices were fabricated using wood kraft pulp based electrodes. As conducting material for the semitransparent electrode, silver nanowires (AgNWs) were used. They were absorbed by the cellulose natural hydroxyl (OH) group. Alternatively, also colloidal graphene-oxide (GO) were investigated as potential candidate, but

the considerably low obtained conductivities were disappointing. The organic semiconductor active layers were deposited by simple drop-casting deposition. As second electrode, aluminum (Al) was used. The according devices with a blend of *poly(3-hexylthiophene-2,5-diyl)* and *phenyl-C61-butyric acid methyl ester* (P3HT:$PC_{60}BM$) as active layer show decent performance with fill factors near 35 % and open circuit voltage of 0.2 V without optimization.

1.2. Cellulose

Paper is one of the most commonly used materials in the world. It would be hard to imagine a society without it. Beside its use for newspapers, books, packaging, toilette paper and so on, it is also used in electronics. There it finds its purpose mainly as an insulator in capacitors and transformers. Recently, attempts were done to fabricate more complex systems. Therefore common printing techniques were used. They allow the realization of more manifold devices, such as sensors, memory devices, radio-frequency identification (RFID) tags, thermo-chromic displays and so on [2, 3, 4]. Also various approaches to gain electrically conductive paper were made. These were accomplished via coating, infiltration or lamination of dispersible or soluble conductors. Conjugated organics, like graphene, carbon nanotubes or polymers were used as conductive material and also conductive oxides or various metals [5, 6].

1.2.1. History and development of paper

Paper history goes back almost 2000 years. Ts'ai-Lun is recorded as the inventor of paper and a paper making process. He presented it around 109 A.D. to the Chinese Emperor. Nevertheless, there may have been paper making even earlier. Due to archaeological investigations its invention is dated 200 years earlier. It took until the 10th centuries to reach Europe. Due to politics and religion it required a few more centuries to establish. However, the invention of the printing press in the mid 15th century paper made its breakthrough [7].
Throughout time, paper was produced e.g. from bamboo, hemp and flax, later on from hemp-, cotton- and linen-rags. Due to industrialization and the increasing

request of paper, new materials had to be found. In 1844 the German inventor Friedrich Gottlob Keller invented the wood pulp process. This process made the use of wood for paper making possible [8].
Unfortunately, paper produced by the wood pulp process contains all components of wood. For that reason it possesses some unwanted properties. For example it appears in a yellowish color. This is caused by the lignin contained in wood. To eliminate these disadvantages, chemical processes were necessary. The Kraft-process (also sulfate process) is one of the more important ones. Due to this chemical process one manages to break the bonds between lignin and cellulose. This is established by a mixture of sodium hydroxide and sodium sulfide, also known as "white liquor". Combined with additional bleaching processes the Kraft-process evolved to be the main process in paper making industry [9].
Todays paper industry plays an important role in global economy. In Austria alone, there are more than 8000 employees. Worldwide hundred thousands of people work in paper industries. They produce more than 166 000 000 tons of pulp and more than 400 000 000 tons of paper per year [10].

1.2.2. Wood pulp to cellulose

Cellulose is not only a part of wood but it also appears in other plants and lifeforms, like grass, sea weeds or bacterias. It is therefore the most abundant natural

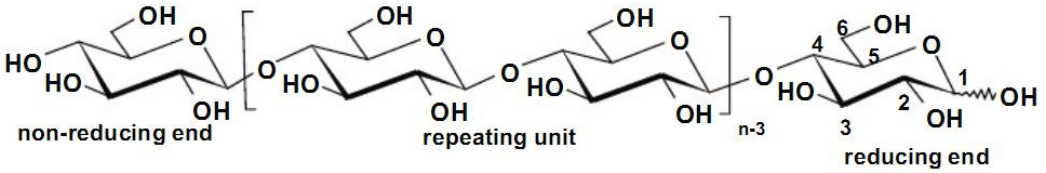

Figure 1.1.: Repetition unit (cellobiose) of a cellulose molecule and its reducing and non-reducing ends. From literature [11].

polymer. Cellulose consists of carbon (C), oxygen (O) and hydrogen (H). Thereof a strictly linear homopolymer chain is formed by anhydroglucose units, which are linked by β-1,4-glycosidic bonds. Each repeating unit contains two anhydroglucose units. Depending on the source material, these so called "cellobioses" get repeated from 3 000 up to 15 000 times. The number of repetitions is understood

as the degree of polymerisation. The cellulose molecules are enclosed with a re-

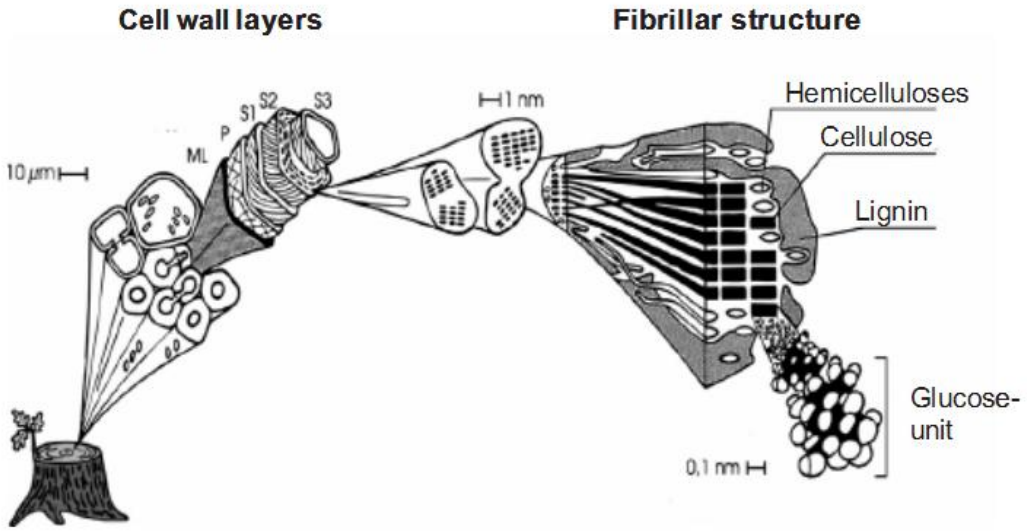

Figure 1.2.: Schematic representation of a wood cell, showing the cell wall layers and the microfibril structure. From literature [11].

ducing and a non-reducing end. In Figure 1.1 the structure of a cellulose molecule is shown. The hydroxyl groups attached at the carbons 2, 3 and 6 are free for reactions [11].

For paper, cellulose is mainly extracted from wood pulp. It is more or less uniform in all types of wood. Besides cellulose, lignin and hemicellulose are two major parts in wood pulp. Their composition varies in different wood types. In Figure 1.2 a schematic description of a wood cell is illustrated. It consists of several different layers. The middle lamella (ML) glues the different cells together. It is expandable and free of cellulose. The inner layers - primary layer (P) and the secondary walls (S1, S2 and S3) - are crisscrossed by microfibrils. The microfibrils mainly consist of cellulose molecules. Due to hydrogen bonds, they form alternating amorphous and crystalline regions. Hemicellulose and lignin complete the microfibrils.

1.3. Organic semiconductors

Under organic semiconductors one understands carbon (C) based compounds that show semiconducting behavior. In general, they feature alternating single and

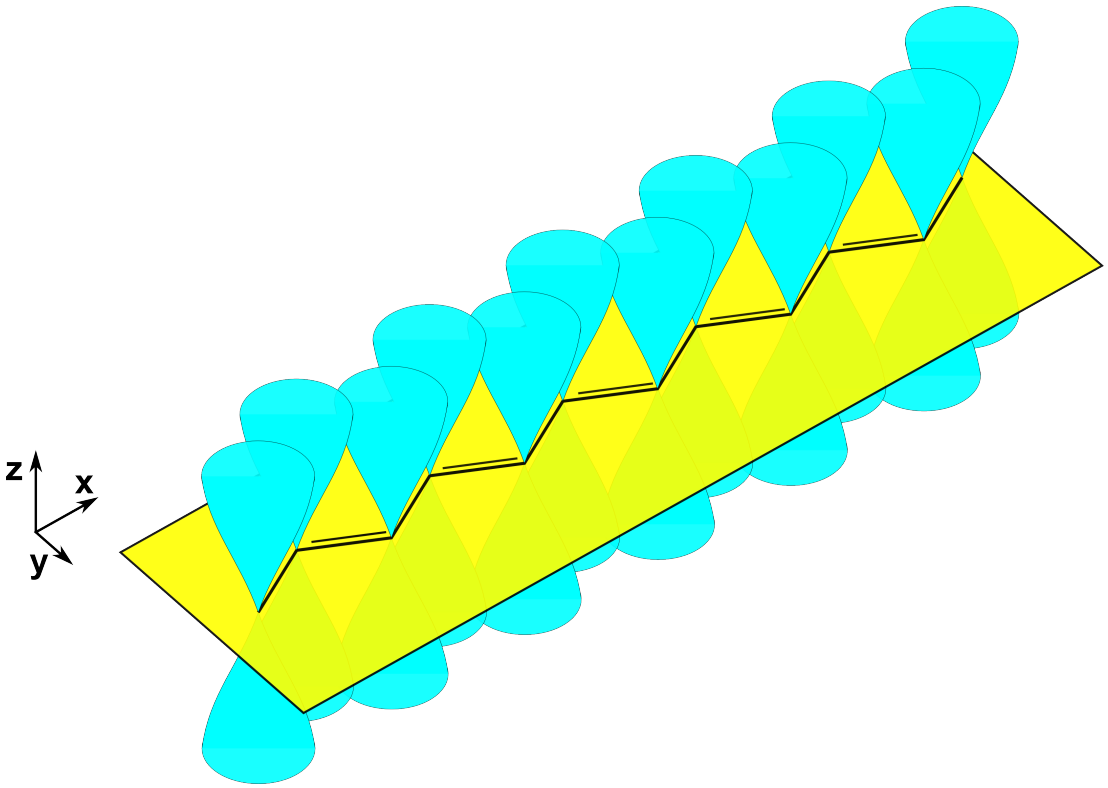

Figure 1.3.: Conjugated backbone of an organic molecule (polyacetylene). The molecular plane is drawn yellow. The overlapping p_z orbitals which form the π orbital are illustrated with blue color. The black lines signify single and double bonds. Adapted from literature [12] created with [13].

double bonds between the carbon atoms. This alternation results in overlapping p_z orbitals, called conjugated orbitals. In Figure 1.3 the conjugated backbone of such a molecule is shown. The conjugation is a results of the formation of three sp^2 hybridized orbitals and one unhybridized orbital. The unhybridized orbital is referred to as p_z orbital. The sp^2 orbitals are located in the xy-plane (molecular plane) and form σ-bonds. The p_z orbital stands orthogonal to them and form π-bonds. The formed π-orbitals overlap with their neighboring π-orbitals. The Electrons in this π-orbitals are spatially delocalized along the molecular backbone. This means that the electrons cannot be dedicated to a specific carbon

atom, but rather form an electron cloud around the molecule. The overlapping π-orbitals are also referred to as "conjugation". Depending on the molecular structure, conjugation can expand over the whole molecule. Therefore the electrons can be delocalized over a wide area. [12, 14]
An unexcited electron will be in an energetically favorable state. This is the ground state. The unexcited electrons fill-up the orbitals with low binding energy. Each orbital contains two electrons with a spin antiparallel to each other. The electrons fill-up the orbitals up to the HOMO, the Highest Occupied Molecular Orbital. The next highest molecular orbital is the LUMO. LUMO therefore stands for Lowest Unoccupied Molecular Orbital. The difference in energy between HOMO and LUMO typically is between 1.5 and 3.5 eV. This is also referred to as band gap. In analogy HOMO and LUMO are often understood as the organic equivalent to the valence and the conducting band in inorganic semiconductors. They play a significant role for the electrical and optical properties of organic semiconductors. [12]
Organic thin films seldom appear in mono-crystalline form. Because of their mainly amorphous/short range order character the charge mobility is limited. For charge transport an electron needs to be lifted to the LUMO by an energy supply (e.g. absorption of a photon). Therefore the energy needs to be equal/higher as the band gap energy. Since band-like transport, is limited to ordered systems, charge transport in organics is dominated by hopping transport. Thereby the electron jumps from the LUMO of one molecule/polymer segment to the LUMO of its neighbor. This is enabled by thermal energy, therefor called "thermally assisted hopping". In analogy, hole transport occurs by hopping between the HOMOs of neighboring molecules/polymer segments.
In general, organic semiconductor materials are chemically synthesized materials. Their size, solubility, components, etc. as well as their electrical and optical properties can be tuned by chemical modifications. This is also their main advantage compared to inorganic semiconductors.

1.4. Organic devices

On the basis of organic semiconductors different kinds of devices can be realized. For example light emitting diodes, photovoltaic cells, transistors and memory devices, just to mention some. Organic photovoltaic cells bear the potential for future large scale power production, using environmentally save and abundant materials. Due to the high absorption rate of organic semiconductors, efficient thin film cells can be produced with only 100 nm thickness. Hence also the production of mechanically bendable solar cells is possible.

1.4.1. Device geometry of organic photovoltaic cells

Throughout time, different device structures for organic photovoltaic (OPV) cells have been developed. The three main geometries will be described in

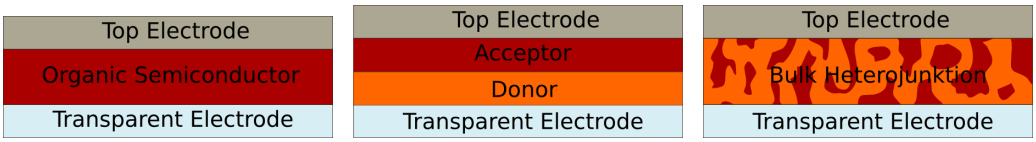

(a) (b) (c)

Figure 1.4.: Schematic illustration of the device geometry of organic photovoltaic cells. (a) Single layer device: An organic semiconductor is sandwiched between two electrodes; (b) Bilayer device: A stack consisting of a donor and an acceptor material between two electrodes; (c) Bulk-heterojunction device: A blend of donor and acceptor materials is sandwiched between two electrodes.

the following. Therefore one differentiates between single layer, bilayer (planar-heterojunction) and bulk-heterojunction devices. They are sketched in Figure 1.4. In single layer devices, one organic material is sandwiched between two electrodes (Figure 1.4(a)). Bilayer as well as bulk-heterojunction devices require donor and acceptor materials. Bilayer devices therefore are build-up of two layers. A donor layer is followed by an acceptor layer between two electrodes (Figure 1.4(b)). Bulk-heterojunction solar cells use a blend of donor and acceptor materials as photoactive layer (Figure 1.4(c)). For all devices, electrodes with different work-functions are essential. The difference in workfunction induces an electric field between the electrodes. This field is required for charge dissociation.

1.4.2. Functional principle of OPV cells

Photovoltaic devices are energy converters. They transform photo-energy into

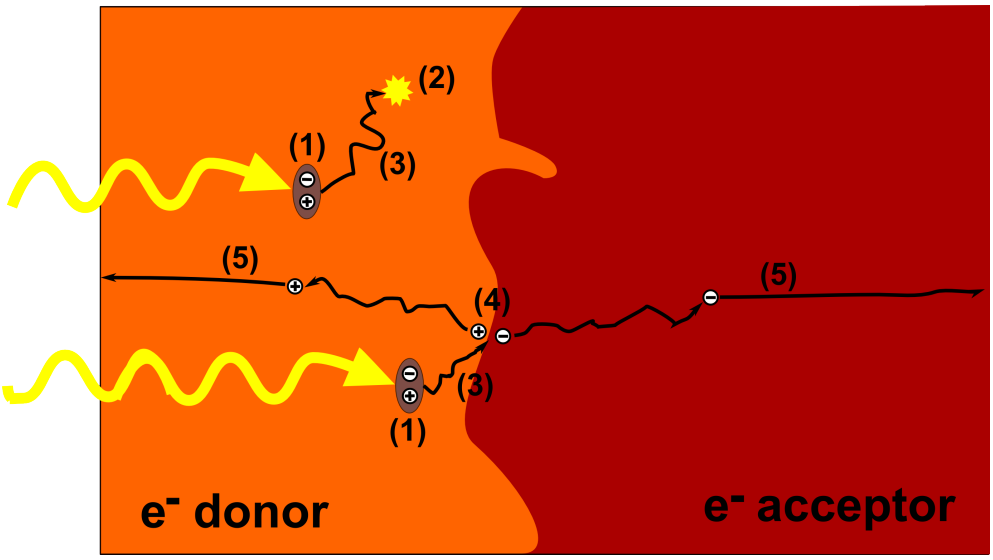

Figure 1.5.: Schematic illustration of the physical processes in a photoactive organic donor/acceptor interface. (1) exciton creation by light absorption; (2) charge recombination (3) exciton dissociation; (4) electron-hole pair separation; (5) charge transport to electrodes; A detailed description, one can find in the text. Adapted from literature [15], created with [13].

electrical energy. In organic solar cells their efficiency depends on four major processes. These effects are schematically illustrated in Figure 1.5. #1 is the photo-absorption and exciton generation. It is quantified by the exciton generation efficiency η_{Abs}. It gives the part of the incoming light which produces excitons. The generated excitons dissociate throughout the material #3). They either happen to recombine #2) or reach the donor/acceptor interface and dissociate into bound electron-hole pairs. (η_{ExDiff}) is the rate of excitons able to reach the donor/acceptor interface and dissociate into bound electron-hole pairs. It strongly depends on the distance the exciton has to overcome before reaching the donor-acceptor interface. Excitons in organic semiconductors are mostly Frenchel excitons, which are localized to the molecule/polymer segment where they have been created. Therefore they have small diffusion length of $5 - 30$ nanometers. If they can reach a donor-acceptor interface before recombination (#2), a charge transfer state is formed at the interface. This means, that the

electron is transfered from the LUMO of the donor to the LUMO of the acceptor. The hole remains in the HOMO of the donor. This electron-hole pair is still coulombically bound to the interface. The bonded electron-hole pairs need to be separated into free charge carriers. This is shown in #4 and is referred to as the separation efficiency η_{Sep}. It strongly depends on the workfunction difference between the electrode materials and needs to be higher than the coulomb attraction, which is about 0.4 eV. The last step (#5) is the charge transport to the electrodes. The electron moves through the acceptor to the cathode and the hole through the donor to the anode. η_{Coll} determines the efficiency of bulk transport of the free charges to their respective electrodes and their collection at the same. It is limited by interface and contact resistance. In Equation 1.1 the over all efficiency is shown.

$$\eta = \eta_{Abs} \cdot \eta_{Exdiff} \cdot \eta_{Sep} \cdot \eta_{Coll} \tag{1.1}$$

A big step in increasing the performance of OPV cells was done by inventing donor/acceptor heterojunction devices. The different electron affinities and ion-

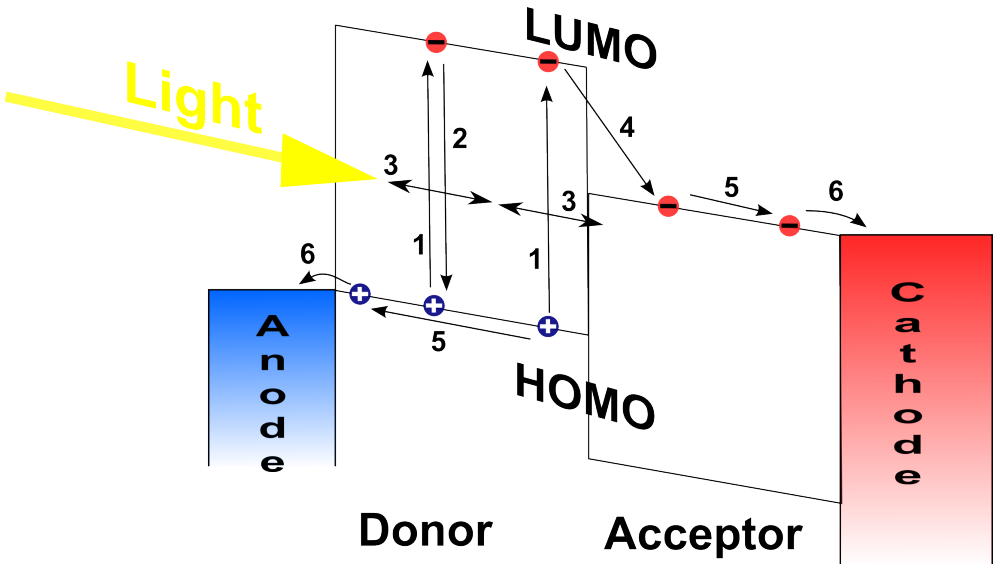

Figure 1.6.: Band diagram of a bilayer OPV cell under illumination. The numerous steps are described in the text. Adapted from literature [16], created with [13]..

ization potentials of the acceptor and the donor material result in a strong local potential at the heterojunction interface. This potential supports exciton dis-

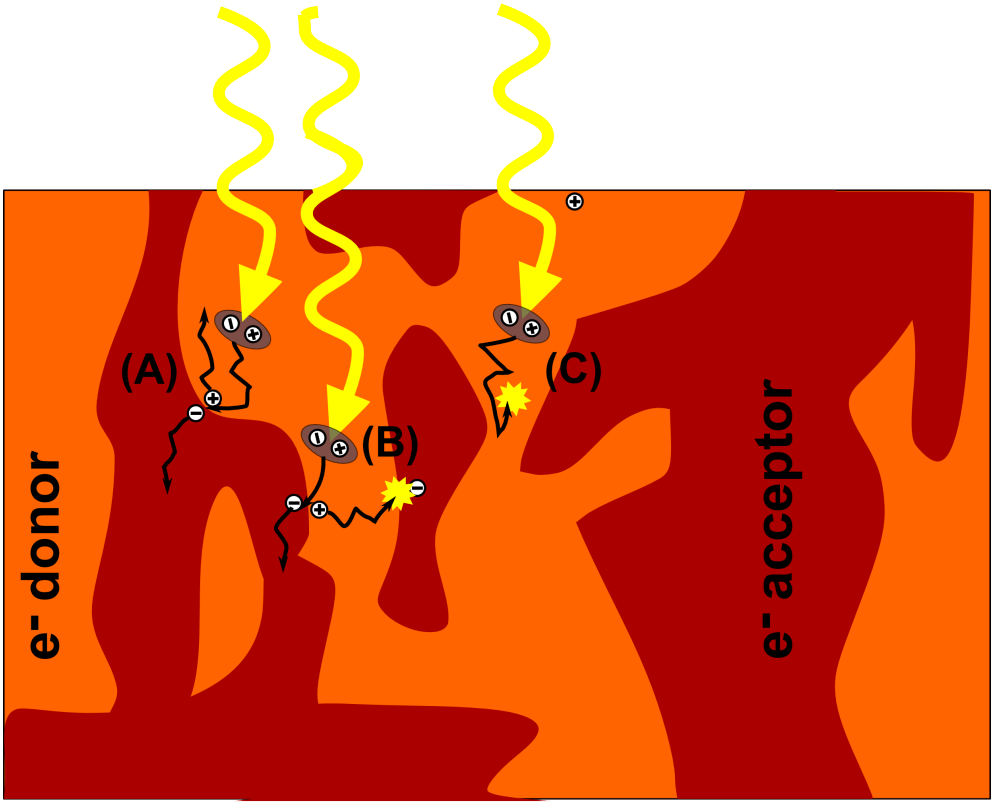

Figure 1.7.: Schematic illustration of the physical processes in a photoactive bulk heterojunktion. (A) Exciton creation by light absorption, exciton dissociation, electron-hole pair separation at the donor acceptor interface, charge transport to electrodes; (B) Exciton creation by light absorption, exciton dissociation, electron-hole pair separation at the donor acceptor interface, charge transport to electrode and recombination with other mobile trapped charges, respectively; (C) Exciton creation by light absorption, exciton dissociation, charge recombination; A detailed description, can be found in the text.

sociation. It is desirable that the potential difference is larger than the exciton binding energy. The electron will be accepted by the material with the larger electron affinity, the acceptor. The material with the lower ionization potential will keep the hole. This is called the donor. The potential differences of the donor/acceptor interface supports the charge separation whereas in single layer devices only the difference in workfunction of the metal electrodes assist. The organic donor/acceptor interface of a bilayer device therefore separates excitons much more efficient than an organic/metal interface of a single layer device. In Figure 1.6 a schematic band diagram of a bilayer device is shown. Side note: The

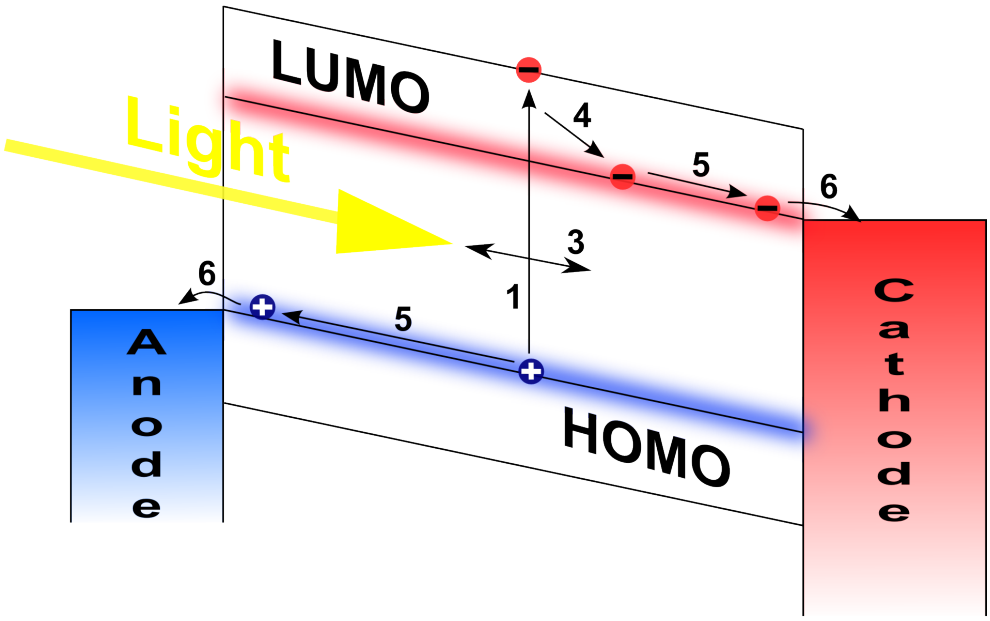

Figure 1.8.: Band diagram of a bulk-heterojunction OPV cell under illumination. The numerous steps are described in the text. Adapted from literature [16], created with [13]..

same process in analogy can also happen for an acceptor. For simplicity only the processes for an excited donor system are highlighted. Molecules inside the device absorb photons. This leads to the excitation of the molecule and to the creation of an exciton (1). The created exciton than starts to defuse throughout the donor (3). If it reaches the donor/acceptor interface charge transfer can take place (4) [16, 17, 18]. The so created metastable electron-hole pair is still coulombically bond. To separate the charge carriers and transport them through the donor/acceptor (5), an external electric field is necessary. This is provided by the difference in workfunctions of the electrodes [16, 19]. The electron (hole) then is collected at the cathode (anode) (6) and driven into the external electric circuit. Still, instead of diffusing to the donor/acceptor interface the exciton can decay (2). This in general leads to luminescence (radiative recombination). If the exciton is created far away from the donor/acceptor interface, the decay rate increases. Therefore it is favorable to create an exciton near the donor/acceptor interface. This limits the width of the effective light-harvesting layer. Because of the small exciton diffusion length of about 10 nm the performance of single layer and bilayer devices is relatively low. [16]

The introduction of the bulk-heterojunction in the mid 90th was a revolutionary development. In a bulk-heterojunction a donor and an acceptor material are blended together. This leads to donor/acceptor interfaces distributed all over the bulk of the active layer. In Figure 1.7 a bulk-heterojunction blend is sketched. The use of a blend allows length scales of the donor (acceptor) phase similar to the exciton diffusion length. On the other hand, the phase still need to provide interconnected pathways for the charge to reach their respective electrode. Though the main physical processes are the same as in the plane heterojunction, additional effects occur. These three different events are distinguished upon excitation: (A) exciton is created, diffuses to donor/acceptor interface, is effectively dissociated and charges move towards the electrode through their respective material. (B) exciton is created, diffuses to donor/acceptor interface, is effectively dissociated but charges recombine on the way to the electrode with other mobile or with trapped charges. (C) exciton is created but does not reach donor/acceptor interfaces and therefor decays. As in an ideal blend the exciton generation mainly occurs near a donor/acceptor interface, the exciton decay process (C) is drastically reduced. In bulk-heterojunction devices, the charge generation takes place everywhere in the active blend.
In Figure 1.8 a schematic illustration of the effective band diagram of a bulk-heterojunction device is shown. The indicated numbers correspond to the same effects as described above for the bilayer interface. [16]
Implying that each material form continuous pathways from the donor/acceptor interface to the corresponding electrode, the photon-to-electron conversion efficiency increases. This results in a drastic increase of photo-sensitivity and the overall efficiency. [16]

1.4.3. Characterization of OPV cells

To investigate the electrical and photoactive behavior of photovoltaic cells, current density-voltage (J-V) characteristics are used. Usually dark measurements and measurements under illumination are performed. In Figure 1.9 an idealized J-V curve is depict. The dark measurement curve shows the diode behavior of the cell without illumination. Under illumination the curve is shifted downwards (negative current) by the amount of photocurrent J_{PH}. The maximum voltage supplied at $J = 0$ A/cm^2 is the open circuit voltage V_{OC}. This is determined by

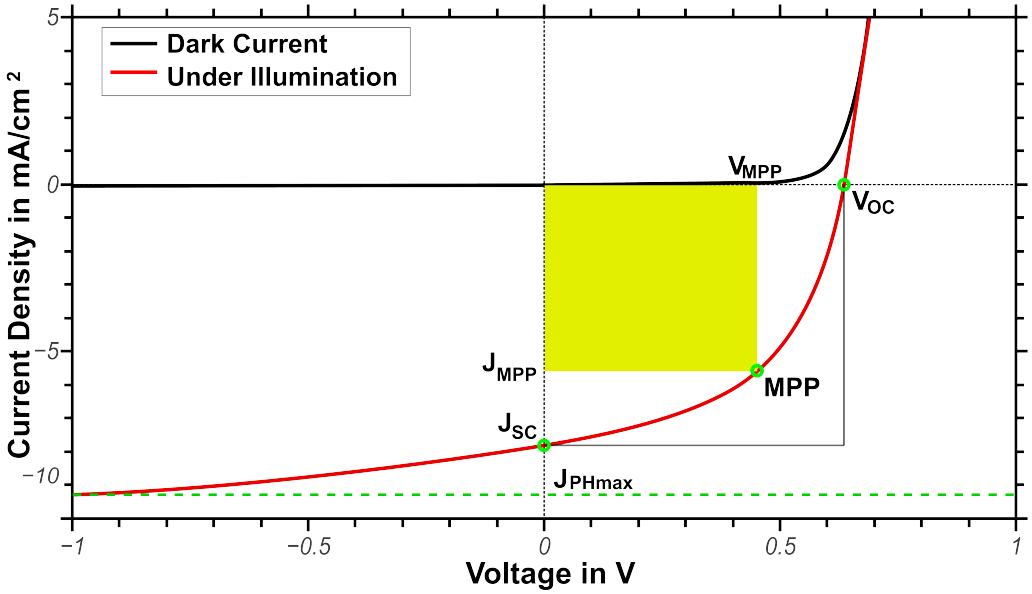

Figure 1.9.: Schematic illustration of a J-V curve of a OPV cell. The marked parameters are described in the text. Created with [13].

the energy difference of the donor's HOMO and the acceptor's LUMO (= effective band gap) and the band banding losses of the ohmic contacts (0.2 V for each contact) [20]. The maximum current at $V = 0$ V is the short circuit current J_{SC}. The maximum of the power P_{max} is given at the maximum power point (MPP).

$$P_{max} = U_{MPP} \cdot I_{MPP} \tag{1.2}$$

It is the product of the maximum power point voltage V_{MPP} and the corresponding current I_{MPP} (Eqn. 1.2). The MPP is shown in Figure 1.9. Therefore the maximum in voltage and current do not correspond with the maximum in power. The fill factor (FF) (Eqn. 1.3) is a measure for the relationship between them, see Eqn. 1.4. The closer the J-V curve is to the shape of a rectangle, the higher is the FF. It is therefore also a measure of rectification of the curve.

$$FF = \frac{U_{MPP} \cdot J_{MPP}}{U_{OC} \cdot J_{SC}} \tag{1.3}$$

$$P_{max} = FF \cdot U_{OC} \cdot J_{SC} \tag{1.4}$$

The measurements with illumination are usually done under AM1.5G conditions. AM1.5G stands for air mass 1.5 global. It simulates the solar spectrum after passing 1.5 times the earth atmosphere which corresponds to a radiation incidence angle of about 48°to the horizon. As standard radiation density $P_{Light} = 100$ mW/cm^2 is defined. The conversion efficiency η calculated under this condition is used for international comparison of photovoltaic cells. In Eqn. 1.5 the formula to calculate the power conversion efficiency is shown.

$$\eta = \frac{FF \cdot U_{OC} \cdot J_{SC}}{P_{Light}} \tag{1.5}$$

Note: During this work no measurements under AM1.5G conditions have be done for technical reasons. The incident power of the light emitting diode (LED) light source was not known. Therefore no power conversion efficiencies was calculated.

2. Experimental

2.1. Materials

In this thesis, different organic and inorganic materials were used. For a better readability of the later sections, the materials and their abbreviations will be introduced below.

As substrate material Monopol X was used. Monopol X is a unrefined soft wood kraft pulp (cellulose). It has been produced by Mondi Frantschach Company and was supplied by Prof. R. Schennach. In the following section I will refer to it as "cellulose".
To fabricate electrically conductive cellulose substrates, graphene oxide (GO), high-conductive grade *poly(3.4-ethylenedioxythiophene):poly(styrenesulfonate)* (PEDOT:PSS) and silver nanowires (AgNWs) were used as conducting material, respectively. All materials were purchased from Sigma-Aldrich and used without further purification. In detail, graphene oxide was available as 2 mg/mL dispersion in H_2O and high conductive PEDOT:PSS as 1.1 wt% in H_2O (pH neutral). Silver nanowires with nominal dimensions of $\varnothing(115 \pm 15)\,\mathrm{nm} \times \mathrm{L}\ (40 \pm 10)\,\mu\mathrm{m}$ were supplied as 0.5 wt% suspension in isopropanol. To reduce the graphene oxide (rGO), *L(+)-ascorbic acid sodium salt* commonly known as vitamin C (198.11 g/mol, $C_6H_7NaO_6$) was used. It was also supplied by Sigma Aldrich and used as received.

As photo-active materials *poly(3-hexylthiophene-2,5-diyl)* (P3HT) and *phenyl-C61-butyric-acid-methyl-ester* ($PC_{60}BM$) were used. P3HT with regioregularity of 91 %, electronic grade, was supplied by Rieke Metals Inc. The $PC_{60}BM$ (99 % purity) was supplied by Ossilla Ltd. Anhydrous o-xylene and chlorobenzene served as solvents. The o-xylene (96.6 % purity; extra dry) and the chlorobenzene (99.8 % purity; extra dry) have been supplied by Acros Organics.

To fabricate the top electrode aluminum wire (99.99 %) was used. In Appendix A specification sheets of the used materials are added.

2.2. Coating methods

To fabricate the conductive substrate and the organic devices, different deposition methods were used. We applied dip-coating to deposit the silver nanowires between and around the cellulose fibers of the cellulose substrate. Drop-coating and/or spin-coating was chosen to cast the different organic layers. Only to prepare the top electrode vacuum deposition had to be used, instead of one of the much simpler coating methods mentioned before.

2.2.1. Dip-coating

For the dip-coating a SDI Nano DIP ND-0407 was used. The ND-0407 dip-coater

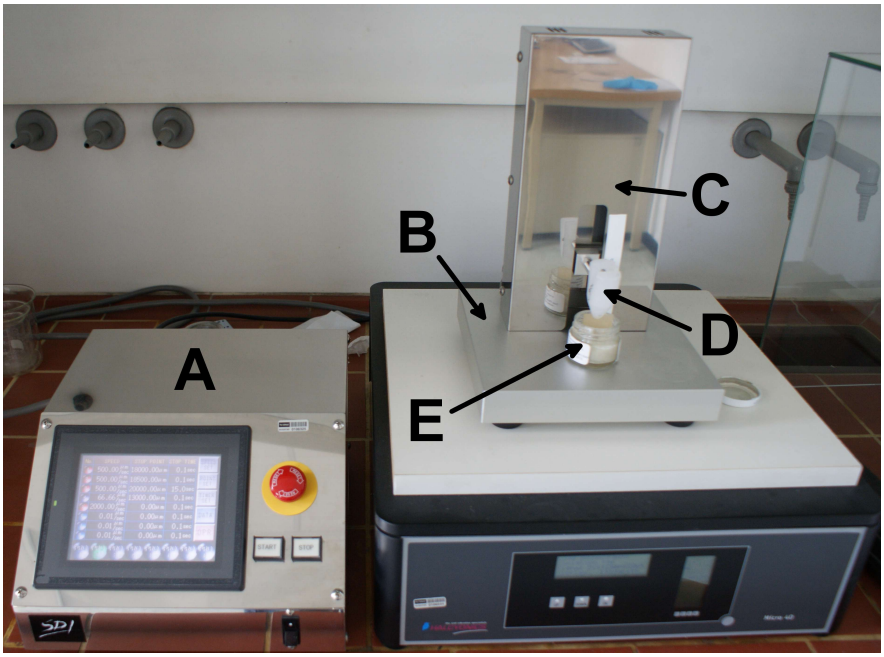

Figure 2.1.: Experimental arrangement of the SDI Nano DIP ND-0407 and the vibration isolation plate inside the fume hood. (A) controller; (B) stage; (C) mobile arm; (D) sample holder clamp; (E) container with solution; (F) Halcyonics active vibration isolation Micro 40 table

is depict in Figure 2.1. The dip-coating operations can be adjusted, using the

touch panel of the controller (A). It allows to individually set the dip-in speed (v_{dip}), the dip-in depth, the waiting time before retraction and the withdrawal speed v_{wd}. During the dip coating the substrate is fixed into a teflon sample holder clamp (D). Here the applied dipping process can be divided into four main steps, illustrated in Figure 2.2. In step #1 the substrate is dipped into the

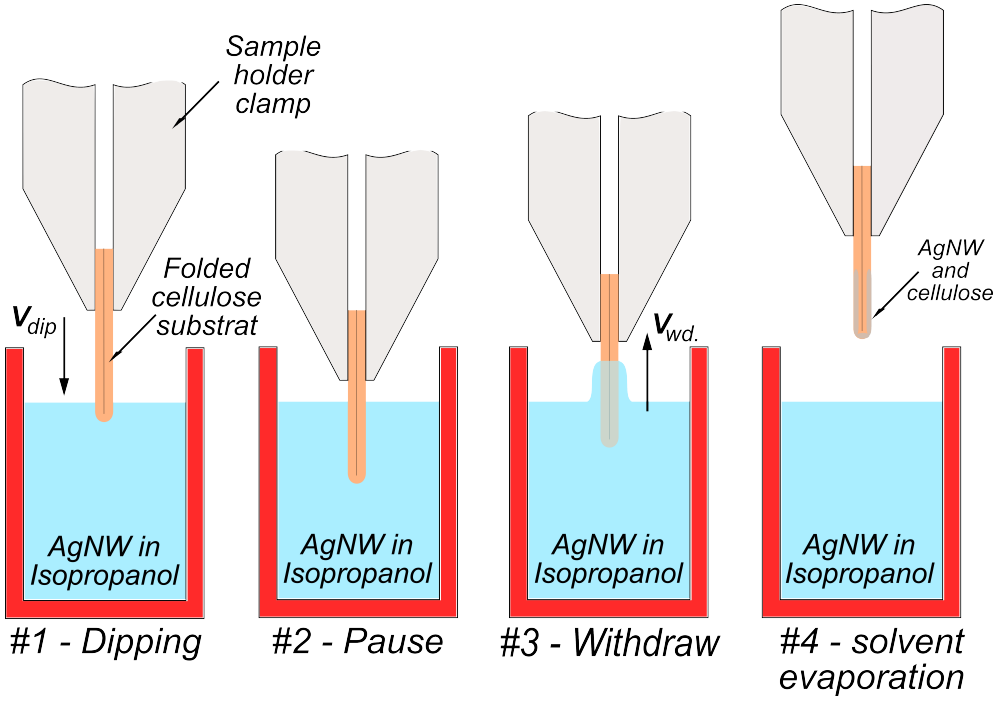

Figure 2.2.: Dip-coat process illustrated as used in the experimental setup. The steps are described in the text.

AgNW-isopropanol solution with v_{dip}. On its maximum dipping depth it stops for a given time (Step #2). Afterwards the substrate is retracted with a v_{wd} (Step #3). During the retraction the actual coating process takes place. As it is described later, the withdrawal speed v_{wd} is essential for the AgNW coverage. In the final step #4 the remaining solvent, in this case isopropanol, evaporates from the substrate.

To minimize vibrations the processing unit was placed on a halcyonics active vibration isolation Micro 40.

2.2.2. Drop-casting

The Royal Society of Chemistry defines drop-casting as:
The application of a thin cover to a sample by depositing consecutive drops of a solution on its surface, and allowing the solvent to evaporate.[21]
During the thesis, drop-casting was executed with a microliter piston pipette with disposable tips. With such pipettes, specific solvent volumes were uniformly

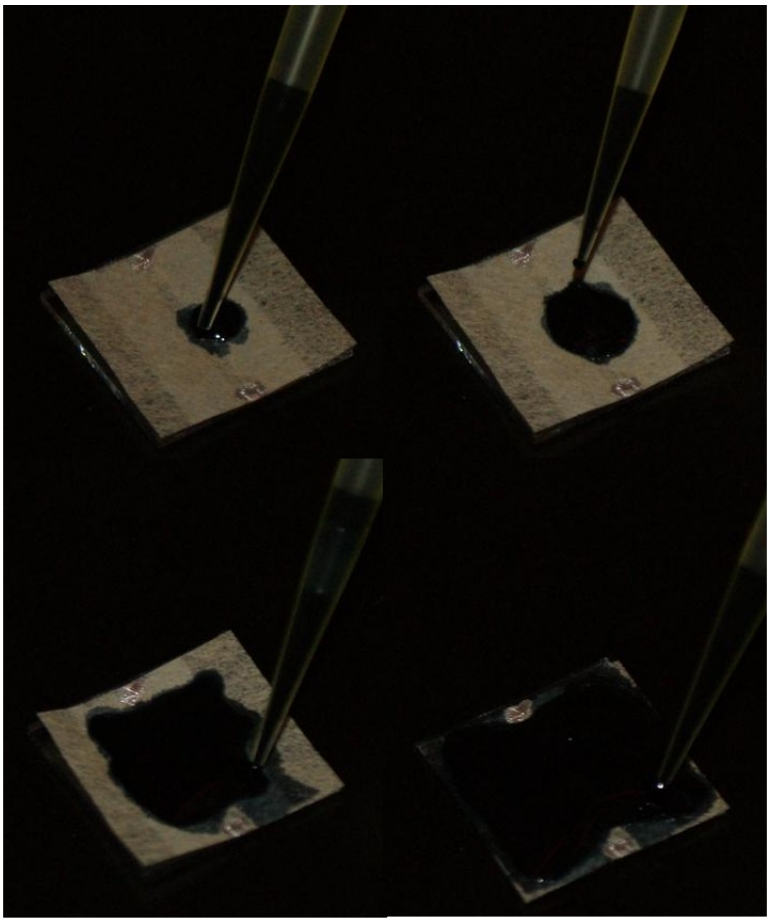

Figure 2.3.: Drop-casting of PEDOT:PSS on a AgNW coated cellulose substrate by micro-pipette.

spread on the substrate. After deposition, the solvent evaporated under heat treatment or at room temperature, respectively. In Figure 2.3 the procedure is shown.

2.2.3. Spin-coating

The spin-coating was either accomplished in air or in argon atmosphere inside the glove box (GB). In air a KW-4A spin-coater from Chemat Technology Inc.

Figure 2.4.: The different spin-coaters used. The right image shows a KW-4A spin-coater placed in the fume hood. The image on the left shows a K.L.M. SCC-200 spin-coater inside the glove box.

was used. The SCC-200 spin-coater from K.L.M. is used in argon atmosphere. Both spin-coaters allow to vary the spin-speed and the spin-time. In Figure 2.4 the two types are shown.

2.2.4. Vacuum deposition

The top contacts of the fabricated devices were applied via thermal evaporation under vacuum. Therefore a build-in thermal evaporator inside the glove box was used. It is shown in Figure 2.5. It consists of a quartz glass cylinder (II), a metal lid (III) and a metal bottom (I) with electrical contacts (A) for two evaporation sources. The lid is equipped with a shutter (C) and a fixture (D) to mount a shadow mask. The shutter is used to cover the mask during the evaporation of organic materials. Additionally a quartz sensor (E) is attached to the lid. This allows to measure the deposited material thickness. The vacuum chamber can be evaporated to a pressure of around $p \approx 10^{-6}$ mbar.
For the evaporation process, samples were placed in a shadow mask, face down.

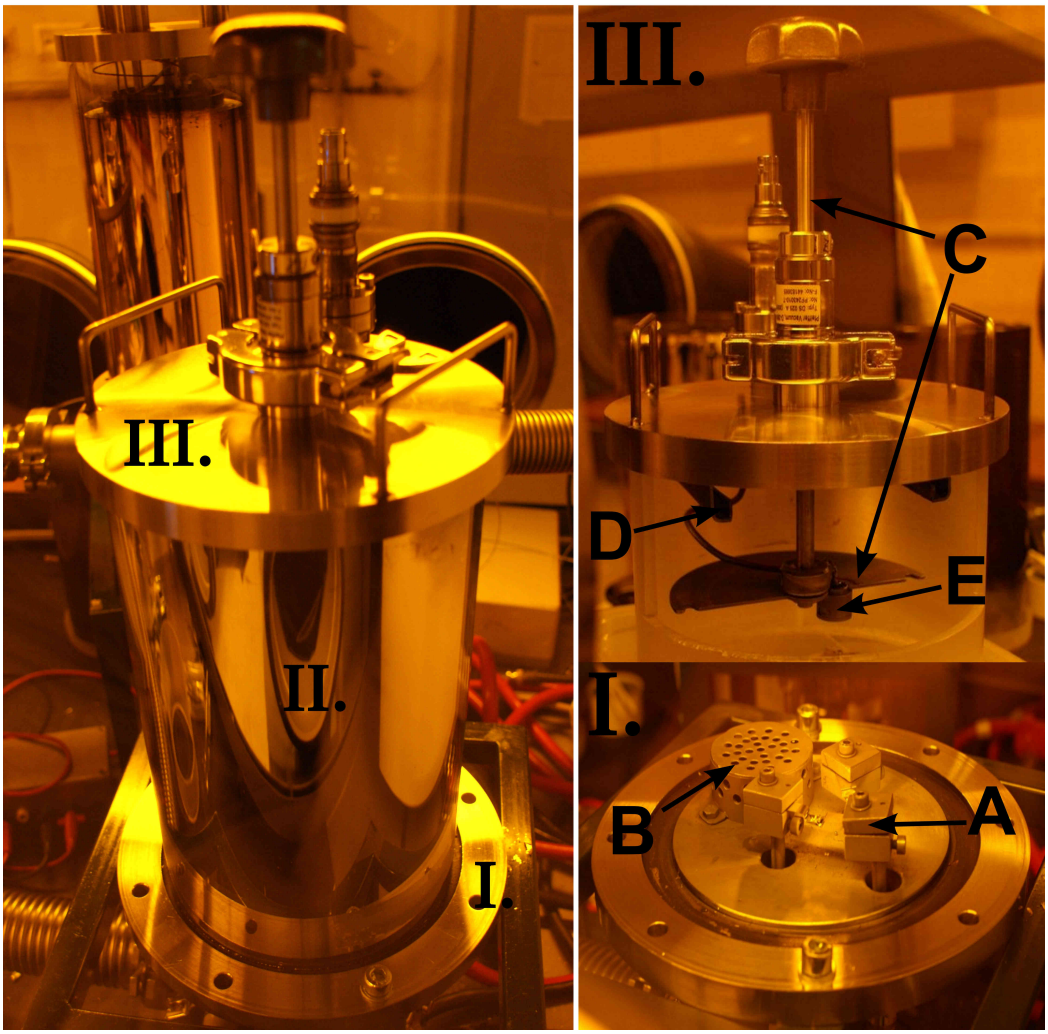

Figure 2.5.: The thermal evaporator "Jaquelin" inside the glove box as a whole, on the left side, and in parts on the right side. The parts are divided in: *I.*) The bottom plate including the electrical contacts (*A*) and the vacuum parts (filter) (*B*). *II.*) A quartz glass cylinder. *III.*) The metal lid including the shutter (*C*), the shadow mask fixture (*D*) and the quartz sensor (*E*).

The used shadow mask is shown in Figure 2.6. Subsequently the mask and the tungsten baskets with aluminum as evaporation source were installed within the vacuum chamber. After evacuation to around $p \approx 10^{-6}$ mbar the aluminum electrode was evaporated on the substrates. The electrode thickness varies for the different devices. It will be mentioned at the corresponding sections.

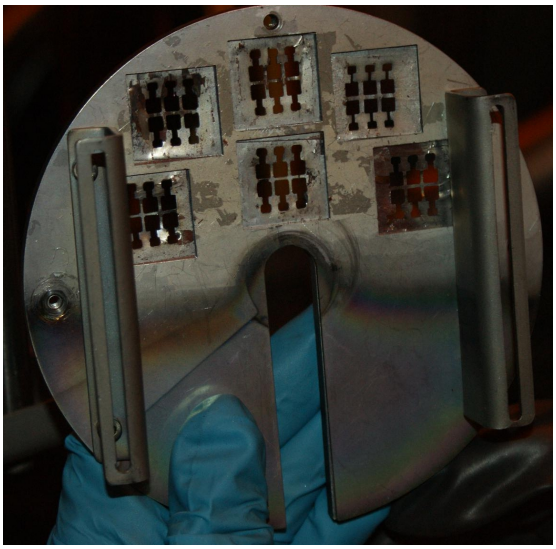

Figure 2.6.: Picture of the shadow mask, used for the evaporation of the top electrodes.

2.3. Analytical methods

2.3.1. Electrical measurements

For electrical characterization two measurement setups were used. One in ambient

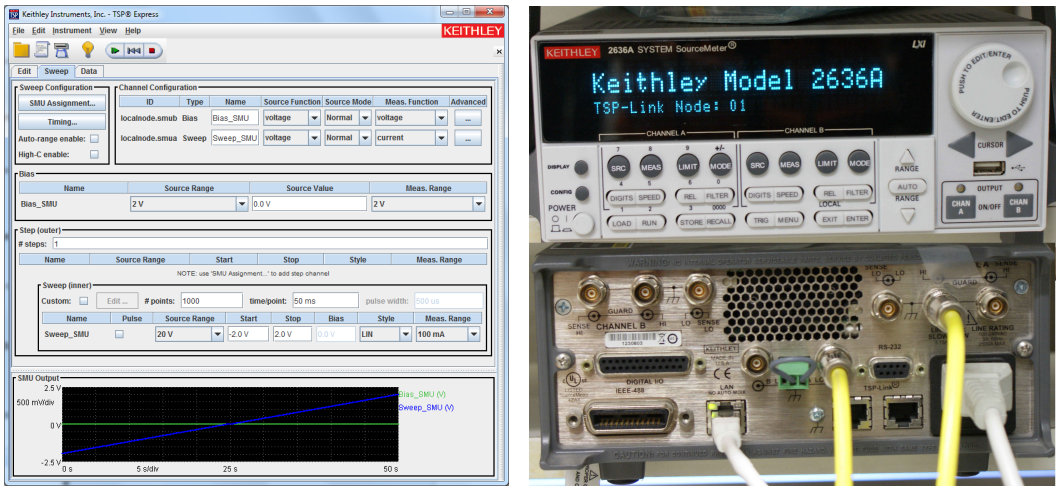

Figure 2.7.: The picture on the left shows a screen shot of TSP®Express. On the right one finds the front (top) and back view (bottom) of a KEITHLEY 2636A SYSTEM SourceMeter®.

atmosphere to measure the substrate resistivity and one inside the glove box

(GB) to characterize the fabricated organic devices. For both measurements a KEITHLEY 2636A SYSTEM SourceMeter® was used. The SourceMeter® was addressed with KEITHLEYs TSP®Express, Version 1.1.1. In Figure 2.7 a screen shot of the program and a picture of the SourceMeter® are shown.

Measurement of the substrate electrical resistance

The electrical resistance of the substrates was measured, using a self-constructed two-point-probe measurement apparatus. It consists of two metal clamps (B)

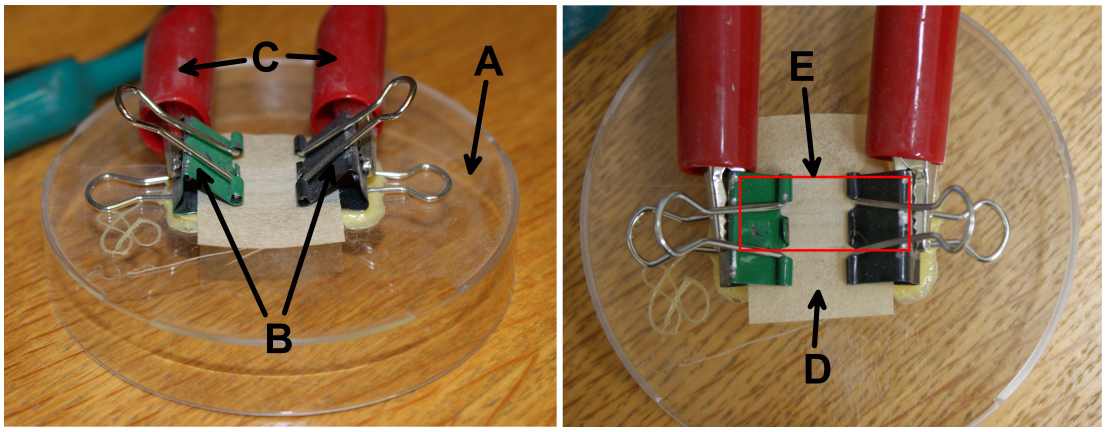

Figure 2.8.: Experimental arrangement of the substrate resistivity measurement apparatus. (A) Electrically isolating bottom; (B) Contact clamps; (C) Crocodile clip connected to the SourceMeter®; (D) cellulose substrate; (E) conductive region of the cellulose substrate

and an electrically isolating bottom plate (A). The clamps are mounted in a distance of $d_R = 1\,\mathrm{cm}$ and were connected to the SourceMeter®via crocodile clips (C) and triaxial cables. The measurement apparatus is depict in Figure 2.8. The electrically conductive region of the cellulose substrate (D) is pointed out by the red rectangle (E) sketched in the right image.
During measurements the conductive cellulose substrates were locked between the two clamps. To gain the substrate resistance, I-V curves were recorded. Every substrate was measured three times. From the I-V curves the mean electrical resistance was calculated, using Ohm's law (Eqn. 2.1). Thereof the mean value of

the three measurements was generated as substrate resistivity R_{Sub}, see Eqn. 2.2.

$$I = \frac{V}{R} \tag{2.1}$$

$$R_{Sub} = \frac{1}{N}\sum_{i}^{N} R_i \tag{2.2}$$

Electrical characterization of organic devices

The characterization of the organic devices was done in *Ar* environment inside the GB. After evaporation of the top electrodes the devices were connected with

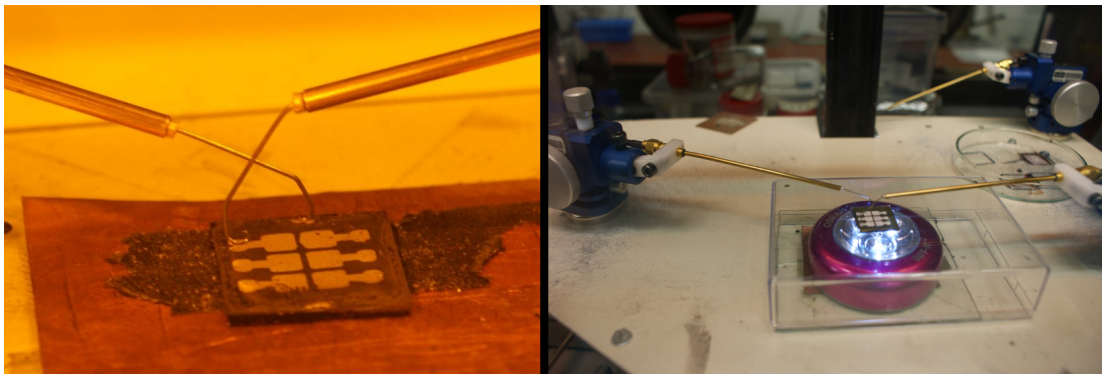

Figure 2.9.: *I-V* characterization setup for organic devices inside the GB. On the left, the measurement with indirect illumination of ambient light is shown. The right picture shows the measurement setup with direct irradiation, using a Osram DOT-it LED white light.

micro-probes. *I-V* curves were recorded using the KEITHLEY SourceMeter® mentioned above.
The electrical characterization of the organic diodes (ODs) was done under ambient light only. To measure photoactivity, the organic photovoltaic devices (OPV) were additionally measured under LED irradiation. Therefore the cells were placed on top of a transparent plastic box. Inside the box a Osram DOT-it LED (0.3 W; 40 lm) light was placed to illuminate the OPV. In Figure 2.9 both measurement setups are illustrated.

2.3.2. Substrate transparency

To evaluate the change in transparency due to AgNW deposition on the cellulose substrate, transmission spectra were taken. Therefore a SHIMADZU UV Spec-

Figure 2.10.: SHIMADZU UV Spectrophotometer UV-1800. The coated substrate (left) and a reference substrate are fixed to the specimen mount with UHU Patafix.

trophotometer UV-1800 was used. In Figure 2.10 the measurement equipment is shown.
The cellulose substrates were fixed to the specimen mount with UHU Patafix. During the measurements the coated side faced the light source. The measurements therefore compares the transparency of conductive cellulose substrates with a pristine cellulose sample.

2.3.3. Optical microscopy

To examine the deposited material on the cellulose substrate, optical microscopy was used. The OLYMPUS BX51 light microscope is equipped with different objectives and a software package to display the images on a computer. Magnifications of 50, 200, 500 up to 1000 times are available. Images can be taken in reflectance and in transmission, respectively. In Figure 2.11 the light microscope is shown on the right and a screenshot of the used program on the left.

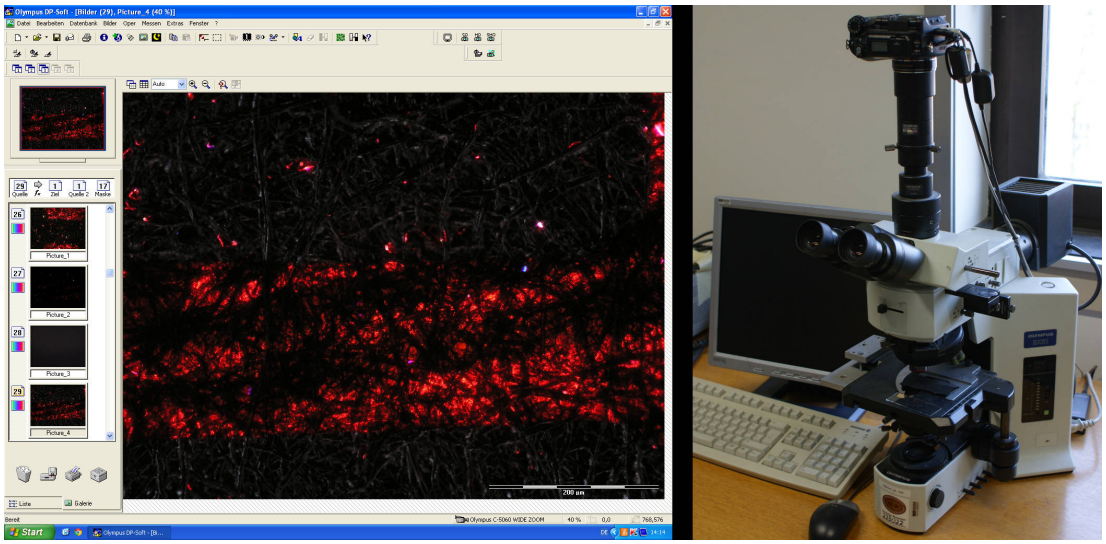

Figure 2.11.: Left handed a screenshot of OLYMPUS DP-Soft is shown. On the right the light microscope with the attached camera (OLYMPUS C-5060) is illustrated.

2.3.4. Scanning electron microscope measurements

For further "optical" analysis, imaging was done with a dual beam microscope (DBM). It consists of a scanning electron microscope (SEM) and a focused ion

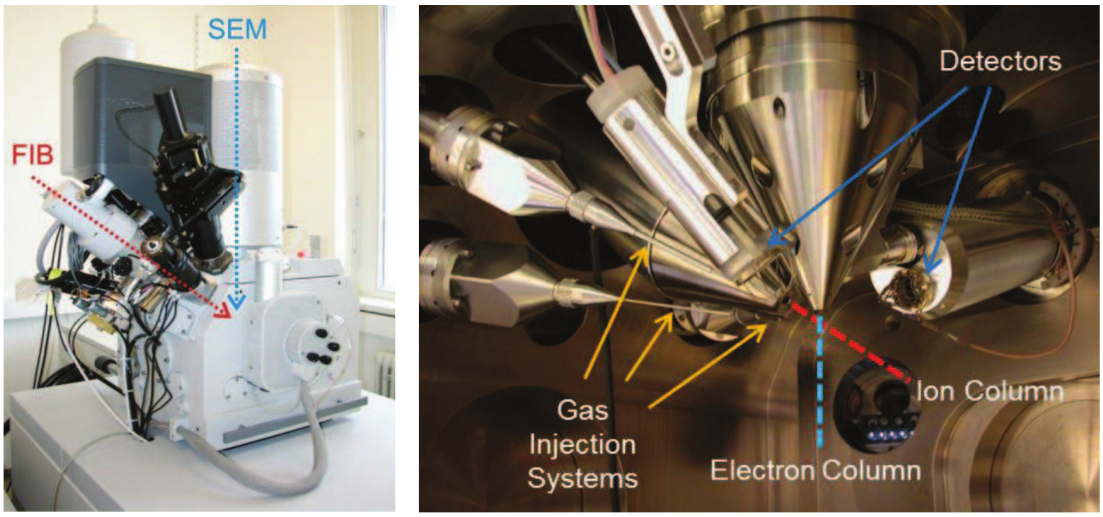

Figure 2.12.: Dual beam microscope located at the FELMI in Graz. On the left side the DBM is shown from the outside. The SEM is arranged vertical, the FIB is inclined by 52°. The image on the right side show the interior of the DBM. The Image was taken from literature [22]

beam (FIB) unit, respectively. The SEM is arranged vertical where as the FIB is inclined by 52° to vertical. For measurements only the SEM was used. Its functional principle can be found in literature [23]. In Figure 2.12 the microscope is shown.

2.3.5. ATR-spectroscopy

For infrared measurements a Bruker ifs v/s FTIR-spectrometer was used. It

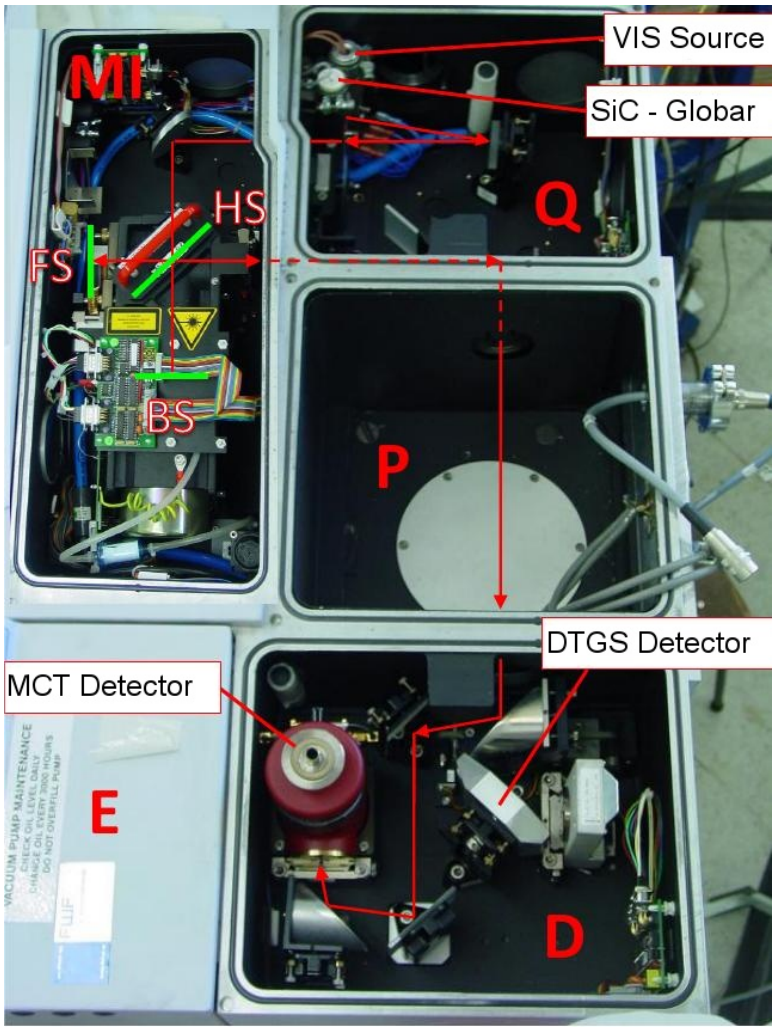

Figure 2.13.: Illustration of the Bruker ifs v/s FTIR-spectrometer. “Q” - source chamber , “MI” - interferometer chamber with the Michelson interferometer (“HS” - semitransparent mirror, “FS” - fixed mirror, “BS” - movable mirror), “P” - probe chamber, “D” - detector chamber, “E” electronic control system; The illustration was adapted from literature [24].

can be utilized for transmission, reflection and attenuated total reflection (ATR) measurements, respectively. In Figure 2.13 the measurement system is shown. The infrared (SiC-Globar) and the visible (VIS) source, including some necessary apertures and mirrors are located in the source chamber "Q". From there, the measurement-beam is directed to the "MI"-chamber where the Michelson interferometer is located. The mirrors of the interferometer are labeled as "HS" (halb-

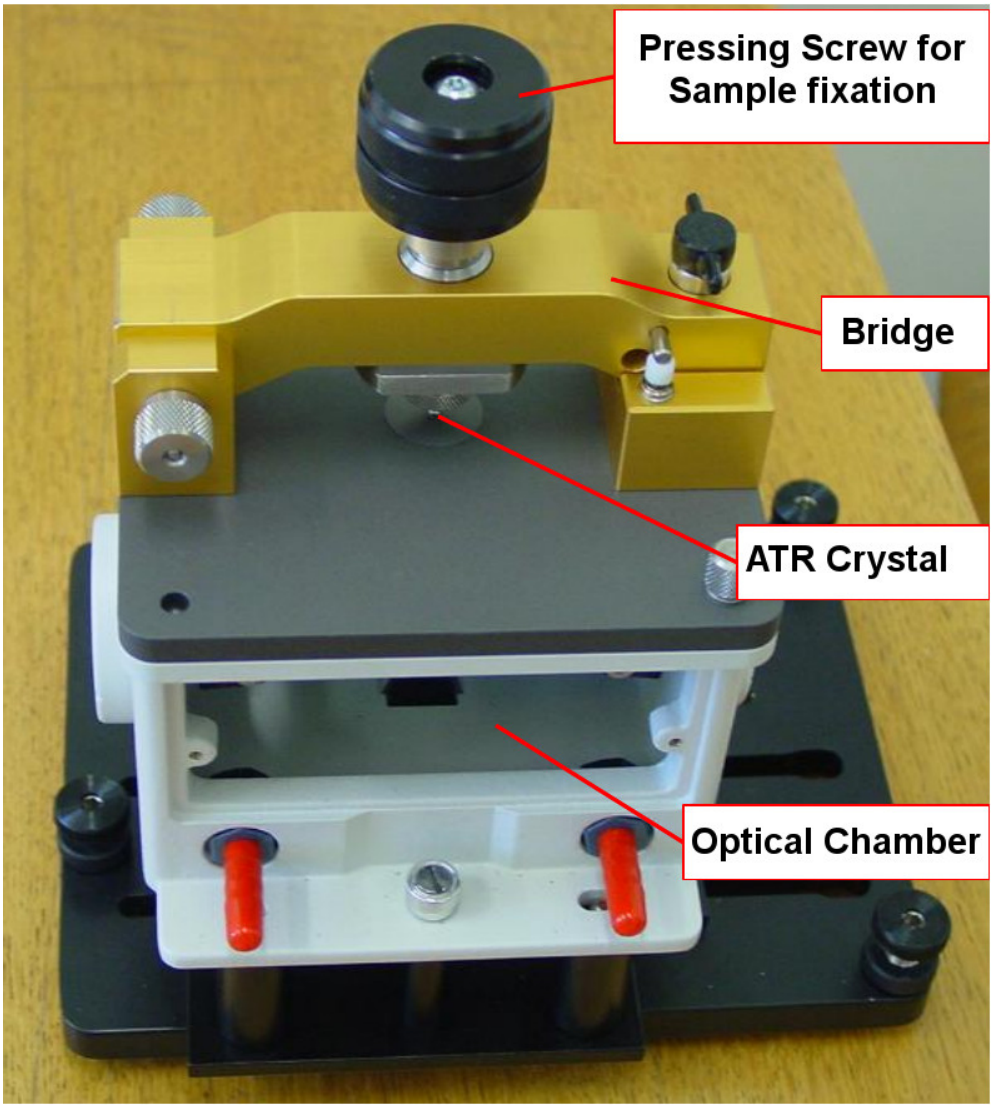

Figure 2.14.: For Bruker ifs v/s FTIR-spectrometer adapted ATR-unit. The illustration was adapted from literature [24].

durchlaessiger Spiegel = semi-transparent mirror), "FS" (feststehender Spiegel = fixed mirror) and "BS" (beweglicher Spiegel = movable mirror), respectively.

From the Michelson interferometer the beam is directed through the sample-chamber “P” into the detector-chamber “D”. The detector chamber is equipped

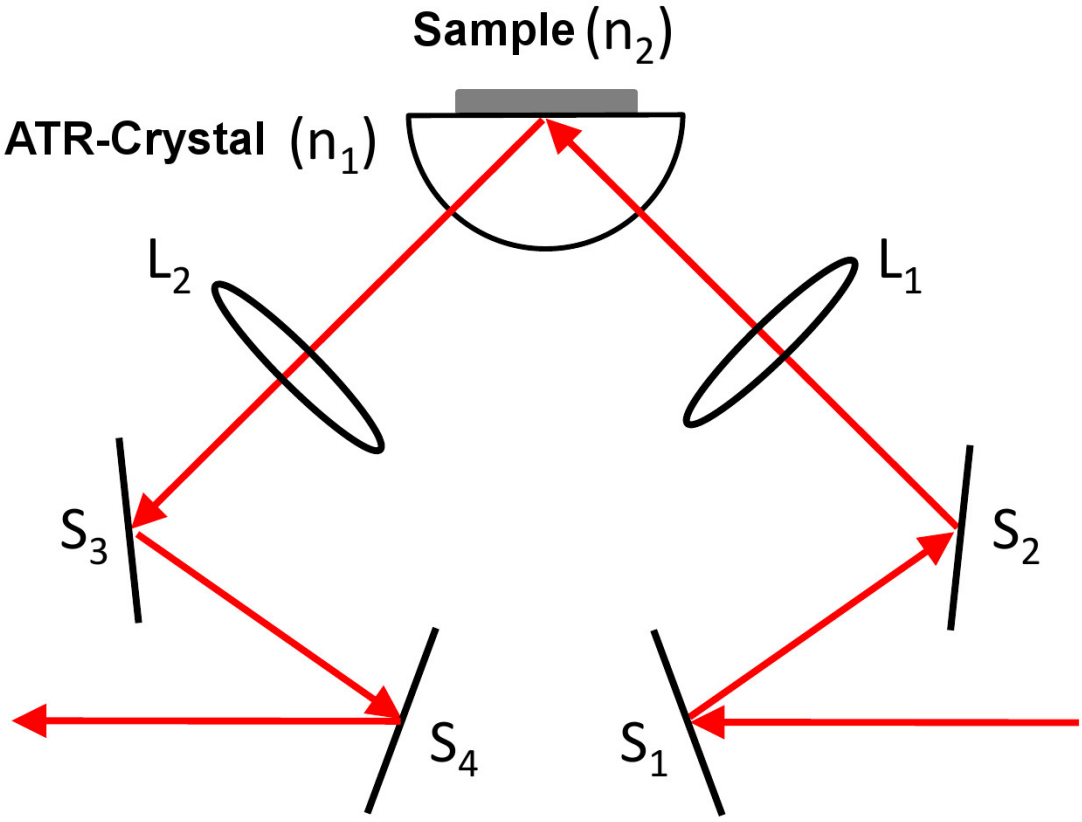

Figure 2.15.: Schematic illustration of the IR-beam path through the ATR-unit. The optical system consists of four mirrors “S”, two convex lenses “L” and a hemispheric diamond ATR-crystal. The illustration was adapted from literature [24].

with a DTGS (deuterated triglycine sulfate) and a MCT (mercury cadmium telluride) detector. In chamber “E” the control system is placed. Further informations on the measurement system and its functional principle can be found in literature [24, 25].
Depending on the type of measurement the probe chamber needs to be equipped with specific measurement units. For attenuated total reflection (ATR) measurements the ATR-unit is used, see Figure 2.14. It is a commercialized unit which was adapted for the Bruker ifs v/s FTIR-spectrometer. The ATR-unit consists of an optical chamber which directs the IR-beam to the ATR-crystal and further on to the detector. In the top plate a hemispheric diamond ATR-crystal is in-

stalled. In Figure 2.15 the optical path inside the ATR is illustrated. Further informations about the system and its adjustment one can find in literature [25]. The samples are fixed to the crystal with the pressing screw that is installed in the bridge. The mechanism is shown in Figure 2.14. ATR measurements allow surface analysis of liquid and solid materials. Therefore the intensity of a reflected IR beam is measured. The attenuation of the reflected beam gives informations about the absorbing medium. In literature [24, 25] the ATR-unit is described in more detail. The figures and drawings of this section were adapted from [24].

3. Electrical conducting cellulose fiber networks

3.1. Experimental

To fabricate electrically conductive cellulose fiber substrates two different approaches were followed. Thereby either reduced graphene oxide or silver nanowires were used for the conductive component. As substrate, unrefined and unbleached soft kraft pulp (Monopol X, Mondi Frantschach, Austria) was used. The kraft pulp fibers were suspended in water. Using a Rapid-Köthen sheet former (DIN EN ISO 5269-2:2004) sheets with a weight of $16\,\mathrm{g/m^2}$ were formed and dried. The substrate will be referred to as "cellulose" in the following.

3.1.1. Reduced graphene oxide as conducting material

Solution preparation

Graphene oxide (GO) sheets dispersed in water (2 mg/mL), were ultrasonicated. To reduce the graphene oxide (rGO), ascorbic acid (vitamin C) was used. The vitamin C was added to the aqueous GO suspension. Subsequently, it was heat treated at temperature of $T_{red.} = 100$℃ and stirred (magnetic stirrer $\backslash U = 300\,\mathrm{rpm}$) during the reduction process. The reduction process is described in literature [26]. In Table 3.1 specific informations on the solution and the reduction parameters are given.

rGO deposition via drop-casting

Cellulose substrates were cut to a size of $(10 \times 20)\,\mathrm{mm^2}$. They were placed on a glass slide. Using a microliter piston pipette the rGO solution was drop-casted

Table 3.1.: Preparation details for reduction of graphene oxide in aqueous solution.

V_{GO} ..... Volume
t_{US} ..... Duration ultrasonic treatment
m_{VC} ..... Amount ascorbic acid
$T_{red.}$ ..... Temperature during reduction
U ..... Stirring speed
$t_{red.}$ ..... Reduction time

Solution	V_{GO} (mL)	t_{US} (h:min)	m_{VC} (mg)	$T_{red.}$ (°C)	U (rpm)	$t_{red.}$ (min)
L407	2	4:15	6.4	100	400	27
L408	2	4:15	5.2	100	400	27
L409	2	4:15	5.9	100	400	30
L410	2	4:15	6.1	100	400	30

Table 3.2.: Preparation details for rGO-conductive cellulose

Solution ..... Composite as described in Table 3.1
V_{drop} ..... Liquid volume dropped onto substrate
T_{dry} ..... Drying temperature
t_{dry} ..... Drying time
R ..... Average resistance over distance of $d = 1\,\mathrm{cm}$

Sample	Solution	V_{drop} (mL)	T_{dry} (°C)	t_{dry} (min)	R (MΩ)
P420	L407	0.3	100	15	1
P421	L407	0.3	100	15	1
P422	L407	0.3	100	15	1
P423	L408	0.3	100	15	10
P424	L408	0.3	100	15	5
P425	L408	0.3	100	15	20
P426	L409	0.3	100	15	—
P427	L409	0.3	100	15	5
P428	L409	0.3	100	15	—
P429	L410	0.3	100	15	100
P430	L410	0.3	100	15	4
P431	L410	0.3	100	15	10

onto the substrate. After deposition it was dried on a hot plate at $T_{dry} = 100$℃. In Table 3.2 the sample preparation parameters are listed.

Characterization

I-V measurements were done to evaluate the sample resistance. Therefore the measurement setup as described in Section 2.3.1 was used. To reduce the uncertainty in measurement, each sample was measured three times. The average sample resistance was calculated at $V = -1\,\mathrm{V}$. For morphological evaluations optical microscopy images were taken. In Section 3.2.1 the results are presented.

3.1.2. Silver nanowires as conducting material

Electrically conductive cellulose sheets were produced, using silver nanowires (AgNWs) as conductive material. The silver nanowires were deposited via dip-coating.

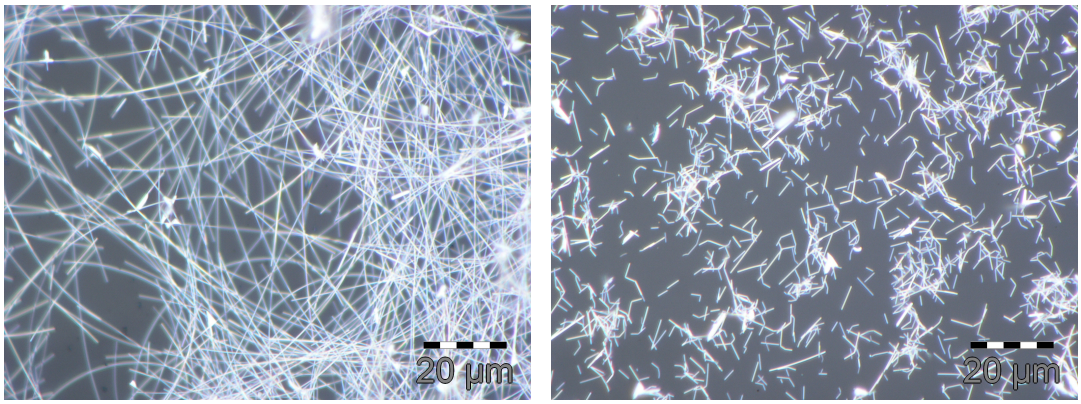

Figure 3.1.: Microscopy images of silver nanowires on glass slides. Right hand side: Untreated AgNWs. On the left, AgNWs after ultrasonication. The ultrasonic treatment led to breaking down to smaller pieces.

Solution preparation

As solution a AgNW suspension 0.5 % in isopropanol as described in Section 2.1 was used. Due to the rapid isopropanol evaporation the suspension was additionally diluted with isopropanol after each dip-coating process. Before coating,

the wires were dispersed in isopropanol by simply shaking the bottle with the suspension. Former attempts using ultrasonic treatment to disperse the AgNWs led to their "destruction". They broke into little pieces which is undesirable for effective charge transport. In Figure 3.1 untreated AgNWs and for several times ultrasonicated AgNWs are shown, respectively.

AgNW deposition via dip-coating

The cellulose sheet was cut into substrates of a size of $(25x40)\,\mathrm{mm}^2$ and folded in half. This is necessary to control the deposition area. Therefore the AgNWs should only be deposited on one side of the substrate and in a specific area. The so prepared substrate was placed into the sample holder clamp of the dip-coater (see Section 2.2.1). The dip-coating process was varied concerning different withdrawal speeds v_{wd}. In Table 3.3 the dip-coating parameters for different samples are listed. After dip-coating, the samples were unfolded and dried in air at room temperature. The prepared samples were then placed and stored between two microscopy slides for flattening and to prevent contamination from the environment until further processing.

Characterization

For quantitative evaluation of the produced samples, I-V measurements were done to evaluate the sample resistance. Therefore the measurement setup as described in Section 2.3.1 was used. To reduce the uncertainty in measurement, each sample was measured three times, with each measurement made on a different sample region. From these data an average sample resistance was computed. To determine the change in optical transparency UV-VIS spectra in respect to pristine cellulose were taken. For morphological studies, optical microscopy and SEM images were taken. In Section 3.2.2 the results can be found.

Table 3.3.: Preparation details for AgNWs-cellulose substrates.

v_{dip} ..... Dip-in speed into solution
t_{stop} ..... Waiting time before retraction
v_{wd} ..... Withdrawal speed from solution

Sample	v_{dip} (μm/s)	t_{stop} (s)	v_{wd} (μm/s)	v_{wd} (mm/min)
P1501	500	30	33.33	2.00
P1502	500	30	33.33	2.00
P1503	500	30	33.33	2.00
P1504	500	15	33.33	2.00
P1505	500	15	33.33	2.00
P1506	500	15	33.33	2.00
P1507	500	30	16.66	1.00
P1508	500	30	16.66	1.00
P1509	500	30	16.66	1.00
P1510	500	15	16.66	1.00
P1511	500	15	16.66	1.00
P1512	500	15	16.66	1.00
P1513	500	30	8.33	0.50
P1514	500	30	8.33	0.50
P1515	500	30	8.33	0.50
P1516	500	15	8.33	0.50
P1517	500	15	8.33	0.50
P1518	500	15	8.33	0.50
P1519	500	30	4.16	0.25
P1520	500	30	4.16	0.25
P1521	500	30	4.16	0.25
P1522	500	15	4.16	0.25
P1523	500	15	4.16	0.25
P1524	500	15	4.16	0.25
P1525	500	30	66.66	4.00
P1526	500	30	66.66	4.00
P1527	500	30	66.66	4.00
P1528	500	15	66.66	4.00
P1529	500	15	66.66	4.00
P1530	500	15	66.66	4.00

3.1.3. Preparation of single cellulose fibers with adsorbed silver nanowires

Fiber preparation

The 16 g/m^2 cellulose substrate was defibrillated in isopropanol for one hour. Using a pair of tweezers, single cellulose fibers were extracted. These pristine fibers serve as reference. Further on, the same cellulose substrate was dipped into a AgNW-isopropanol suspension. Thereby it was coated with AgNWs. From this cellulose substrate, single cellulose fibers coated with AgNWs were extracted for inspection with the same procedure.

Characterization

To verify the presence of AgNWs on the single cellulose fibers, light-optical microscopy images were taken. Fourier transformed infrared spectra were recorded with the attenuated total reflectance (ATR) technique. Therefore a special ATR-device which was adapted to the BRUKER IFS 66v/S spectrometer, was used. The measurement setup is described in Section 2.3.5. In Section 3.2.3 the results are displayed.

3.2. Results and discussion

3.2.1. Conductive cellulose based on reduced graphene oxide

As described in Section 3.1.1 reduced graphene oxide (rGO) was used to fabricate conductive cellulose substrates. The fabrication process was based on a report by Fernández-Merino et al.[26]. They describe the fabrication of free-standing, paper like rGO films with high electrical conductivities. To reduce the GO they used vitamin C.
In Figure 3.2 optical light microscopy images of rGO coated cellulose substrates are shown to demonstrate optical effects. The same sample is shown with top and bottom illumination, respectively. The coated rGO does not adsorb to the cellulose fibers, but forms separated agglomerates instead. Thereby it forms a porous, dark gray and nonuniform layer on top of the cellulose substrate. These

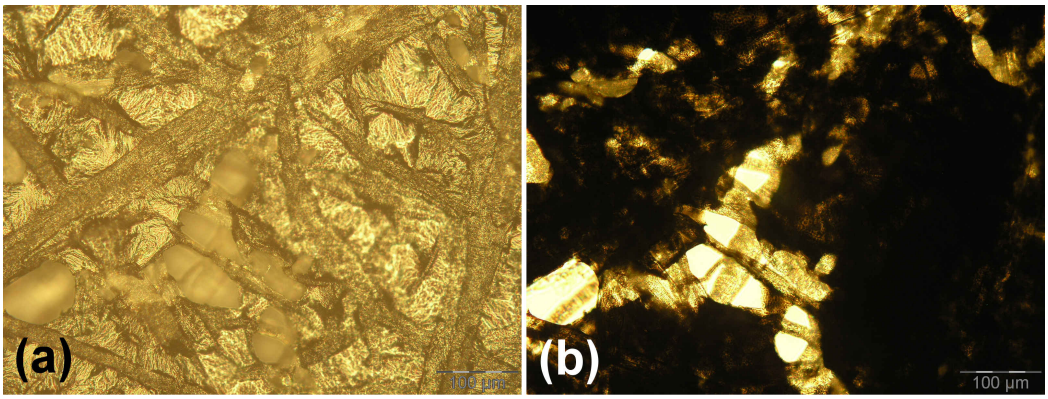

Figure 3.2.: Light microscopy images of reduced graphene oxide (rGO) drop-casted on a cellulose substrate. (a) was taken in reflection, (b) in transmission mode. The different surface textures in (a) indicate more or less isolated rGO islands. In (b) one can identify areas of higher (dark) and lower (bright) rGO occupation.

layer consists of rGO islands which are partly isolated from each other. The different surface textures shown in Figure 3.2(a) are caused by this effect.
In Figure 3.3 optical light microscopy images of two different samples (P420 / P425) are shown. The samples were illuminated from the back. The dark areas show rGO deposits. The bright areas signify uncoated gaps between the deposits. Despite the fact that the samples were prepared almost identical, considerable differences in coverage are observed. The substrate P420 shown in Figure 3.3(a) contains of relatively large, continuous rGO regions. Therefore its resistance is relatively low. It is about $R \approx 1\,\mathrm{M\Omega}$. The substrate resistance increases considerably when the rGO sheet size decreases. This is caused by the weak electrical connections between the single islands. This leads to an increase of resistance when the size of the rGO islands decreases. The sample P425 displayed in Figure 3.3(b) already shows a resistance of 20 times higher magnitude then the one shown in Figure 3.3(a). The rGO-conductive cellulose substrates show rather irreproducible coverage and strong inhomogeneity. As a result, the substrate resistance of the rGO-conductive cellulose substrates varies in the range from 1 to 100 MΩ.

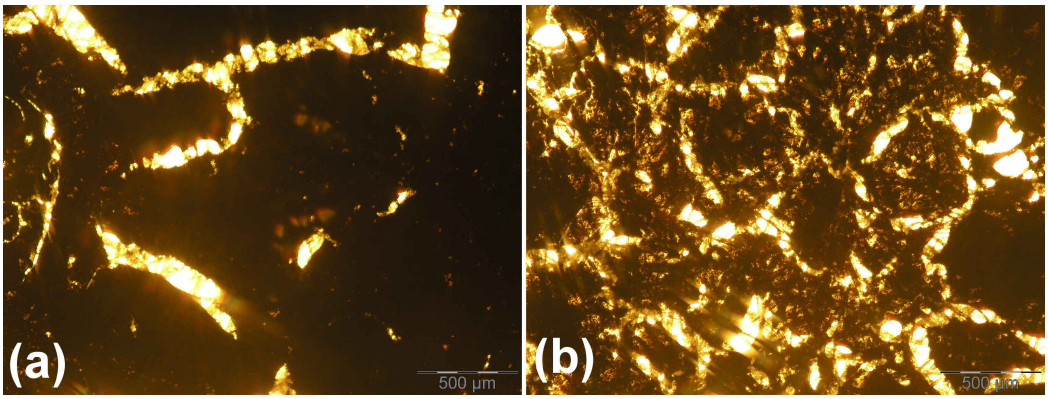

Figure 3.3.: Light microscopy pictures of reduced graphene oxide (rGO) drop-casted on a cellulose substrate. The pictures were taken with back illumination of the samples. In (a) sample P420 and in (b) sample P425 are shown. The samples were almost identically prepared. The dark areas show rGO deposits. The bright areas signify uncoated gaps between the deposits. The rGO layer discontinuity leads to a high substrate resistance.

3.2.2. Conductive cellulose based on silver nanowires

The fabrication process of conductive cellulose fiber networks was described in Section 3.1.2. Thereby the silver nanowires (AgNWs) form conductive networks between and around the cellulose fibers. In Figure 3.4 SEM images of these AgNW networks on a cellulose substrate are presented. This networks are essential for charge transport. The dark lines surrounding the nanowires are due to charging effects. As discussed in detail later (Section 3.2.3), the AgNWs adhere to the cellulose fibers due to chemical interactions with surface groups. The conductive networks are significant to provide charge transport pathways across and throughout the substrate. The more intersecting nanowires participate in the charge transport the lower is the substrate resistance. The nanowire density is adjustable by the coating parameters.
In Figure 3.5 different treated cellulose substrates are presented. In Figure 3.5(a) pristine cellulose is shown. There are obviously no AgNWs present. The pristine cellulose works as an electrical insulator. Figure 3.5(b) shows a cellulose substrate after dip-coating in AgNWs suspension. The withdrawal speed used was $v_{wd} = 4\,\mathrm{mm/min}$. In this sample one can see sporadically distributed AgNWs between the cellulose fibers. These nanowires form networks between and around the fibers. Due to these networks the substrate becomes conductive. The resis-

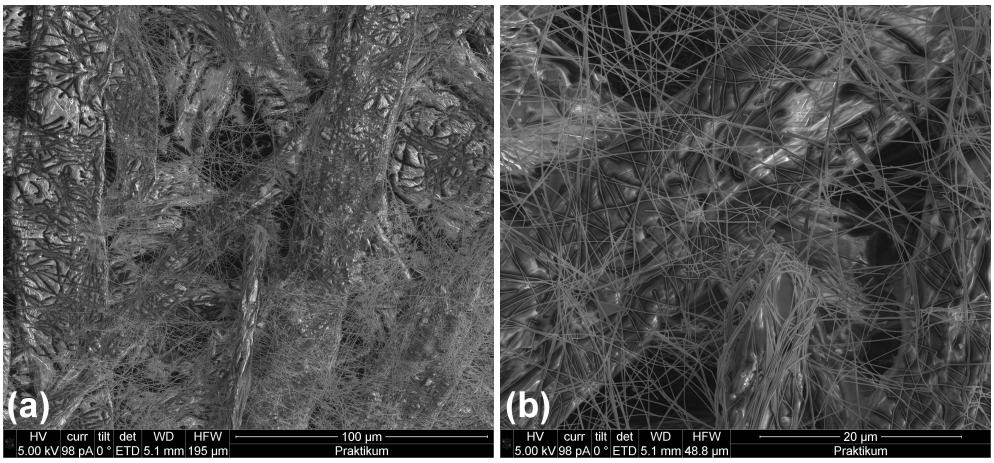

Figure 3.4.: SEM images of Monopol X cellulose coated with silver nanowires. In Figure (a) and (b) details of the substrate are shown with different amplifications. The scale is embedded in the images.

tance over a distance of $d = 1\,\text{cm}$ is in the range of a few hundred ohms. The resistance was determined as described in Section 2.3.1.

Figure 3.5(c) and 3.5(d) show substrates dip-coated with a withdrawal speed of $v_{wd} = 2\,\text{mm/min}$ and $v_{wd} = 0.25\,\text{mm/min}$, respectively. Due to the lower v_{wd}, the AgNW density on the substrate increases. This in consequence leads to a decrease in resistance. The substrate resistance exclusively depends on the nanowire coverage.

In Figure 3.6 the substrate resistance in dependence of the withdrawal speed is shown. Therefore six samples were produced for each withdrawal speed. Each sample was measured three times at different sample regions. From these data the average resistance for each sample was computed and plotted. As clearly visible in Figure 3.6 (magnified in the insert), the resistance increases continuously for withdrawal speeds between $v_{wd} = 0.25\,\text{mm/min}$ and $2\,\text{mm/min}$. The red line marks the resistance of a ITO/Glass substrate supplied by Ossila Ltd. (ITO stands for Indium Tin Oxide.) It was measured with the same method. This shows, that the conductivity of the produced substrates lies in the same range as for commercial ITO based substrates. Nevertheless, for higher withdrawal speeds the resistance increases rapidly, as shown for $v_{wd} = 4\,\text{mm/min}$. This is due to the lower AgNW density. The resulting strong scattering of the resistance is caused by sporadic distribution of the AgNWs on the cellulose substrate, as well as by variations of the cellulose fiber density of the substrate.

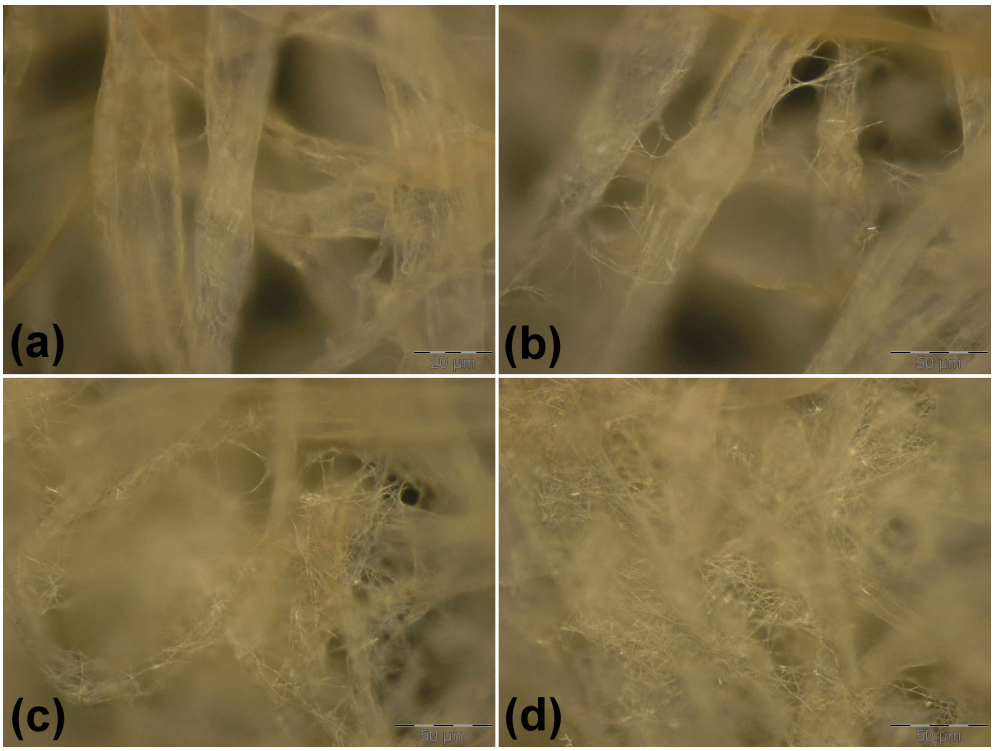

Figure 3.5.: Optical microscopy images of pristine and with silver nanowires coated cellulose (magnification of 500 ×). (a) shows pristine cellulose. The AgNW coated cellulose substrates were dip-coated with withdrawal speeds of (b) $v_{wd} = 4\,\mathrm{mm/min}$ (P1529), (c) $v_{wd} = 2\,\mathrm{mm/min}$ (P1505) and (d) $v_{wd} = 0.25\,\mathrm{mm/min}$ (P1523), respectively.

The increase of AgNW coverage visible in Figures 3.5(a), 3.5(b) and 3.5(c) also affects the substrate transparency. To examine this change in transparency, UV-VIS spectra were recorded. The inset in Figure 3.7 shows the over all transmittance of ITO/Glass and pristine cellulose compared against air as reference. Comparing the two graphs, it is obvious that the cellulose substrate is less transparent for a wide region. The low transmittance of about 10 % for pristine cellulose gives rise to concern that it might be inapplicable as a truly transparent electrode for optoelectronic devices. However, this assumption can be disproved when it is taken into consideration that cellulose does not absorb or reflect the incoming light but scatter it into different directions [27]. Therefore a photoactive device located on the substrate is mainly irradiated by stray light between fibers. Only a small part of the irradiation is caused by direct illumination. Since UV-VIS measurements detect primarily transmitted light, the comparison of cel-

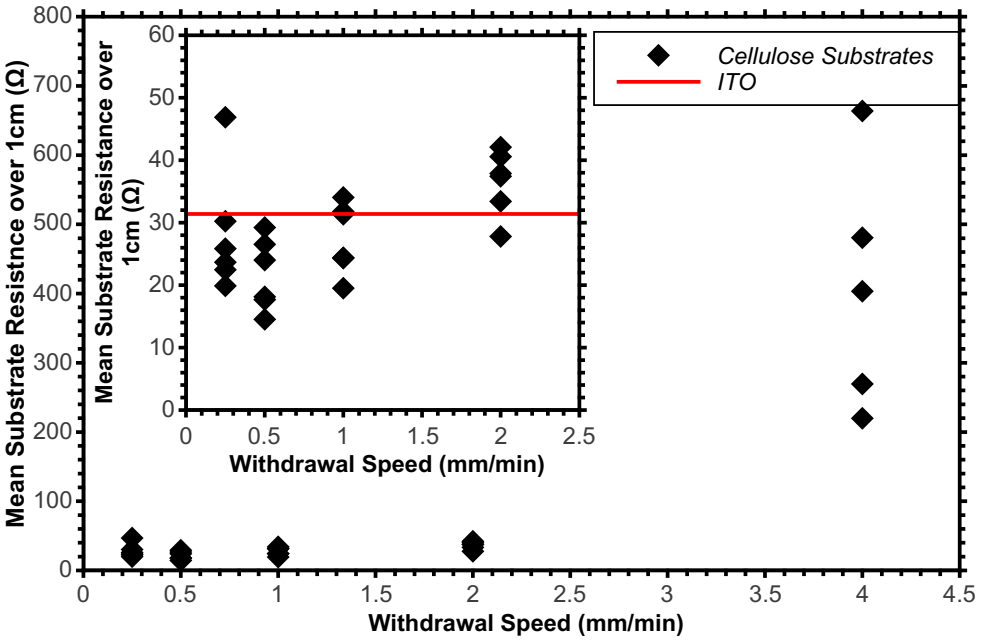

Figure 3.6.: Mean resistance of cellulose fiber network dip-coated in AgNW suspension in dependence of the used withdrawal speed. The inset shows the mean resistance of commercial ITO/glass substrate and the region between $v_{wd} = 0$ to 2.5 mm/min. The particular mean substrate resistance was calculated out of three independent I-V measurements. The voltage used was $V = -1\,\mathrm{V}$.

lulose to air is not meaningful. To determine the effect of the adsorbed nanowires alone, the transparency of conductive cellulose substrates was compared to a pristine cellulose substrate. In Figure 3.7 the transmittance at $\lambda = 550\,\mathrm{nm}$ of several coated cellulose substrates in relation to a pristine cellulose substrate is shown. Therefore, the same samples were used as mentioned above. The transmittance increases with increasing withdrawal speed and therefore with decreasing nanowire presence. For low coverage as for $v_{wd} = 4\,\mathrm{mm/min}$, the light transmitted through the coated substrate lies in the same intensity range as for pristine cellulose. The reason for transparencies nominally higher than 100 % is caused by natural variations in the cellulose substrates. The nanowire density is very low and the variation in transmittance are mainly dominated by the cellulose fiber density of the observed region.

For lower withdrawal speeds the nanowire density increases and its effect on the substrate transparency dominates. Hence, the relative transparency decreases down to about 50 % in average, for low withdrawal speeds. This is shown in Figure

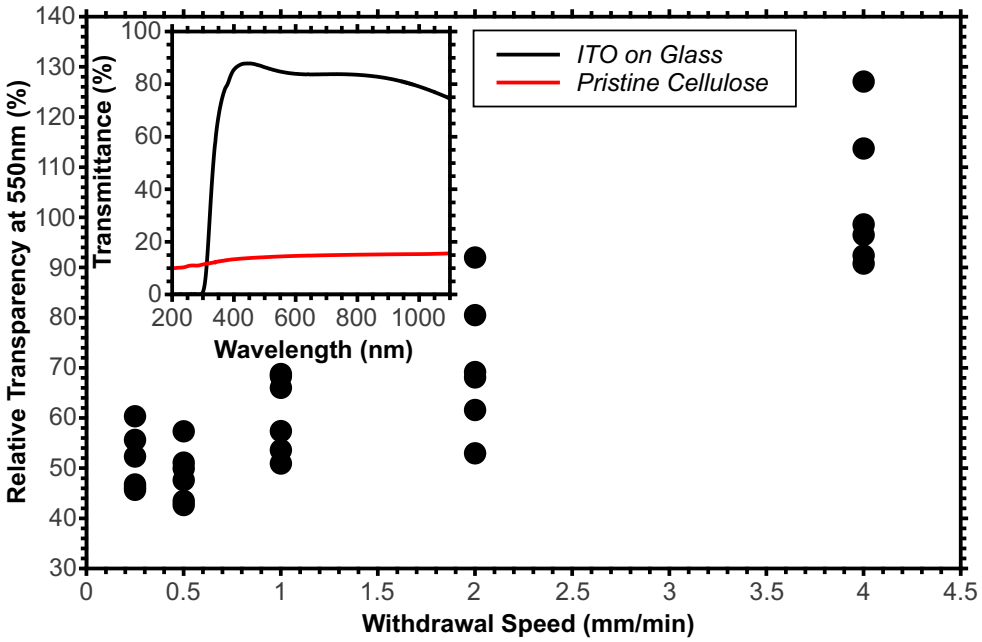

Figure 3.7.: Relative substrate transparency for different samples at $\lambda = 550\,\text{nm}$ in dependence of the withdrawal speed. The inset shows the over all transmittance of ITO/glass and pristine cellulose compared against air.

3.7 for withdrawal speeds of 1.00, 0.50 and 0.25 mm/min. There the transparency is mainly dominated by the AgNW density. Therefore the natural variations of the cellulose fiber density is insignificant. For fast speeds as $v_{wd} = 2.00\,\text{mm/min}$ the AgNW density decreases and vise versa the average relative transparency increases to about 70 %. Again, the fluctuations in transparency of these samples are caused by natural variations of the cellulose substrate. Hence, the cellulose fiber density gains in importance for transparency when the AgNW density decreases.

The transmission spectra of AgNW coated cellulose substrates relative to a pristine cellulose substrate is shown in Figure 3.8. It shows constant behavior over a wide region for wavelength $\lambda > 450\,\text{nm}$. The decrease in transmission is mainly caused by reflection behavior of the coated AgNWs [28]. The thicker the nanowire network, the higher is the reflectivity. Hence a decrease of transmittance appears with decreasing withdrawal speed. For wavelength below $\lambda = 450\,\text{nm}$, plasmon absorption is the predominant effect. It has its maximum resonance at about $\lambda = 360\,\text{nm}$ where it leads to a minimum in transmission. This plasmon absorption also causes the grayish appearance of the coated nanowires [28, 29]. The

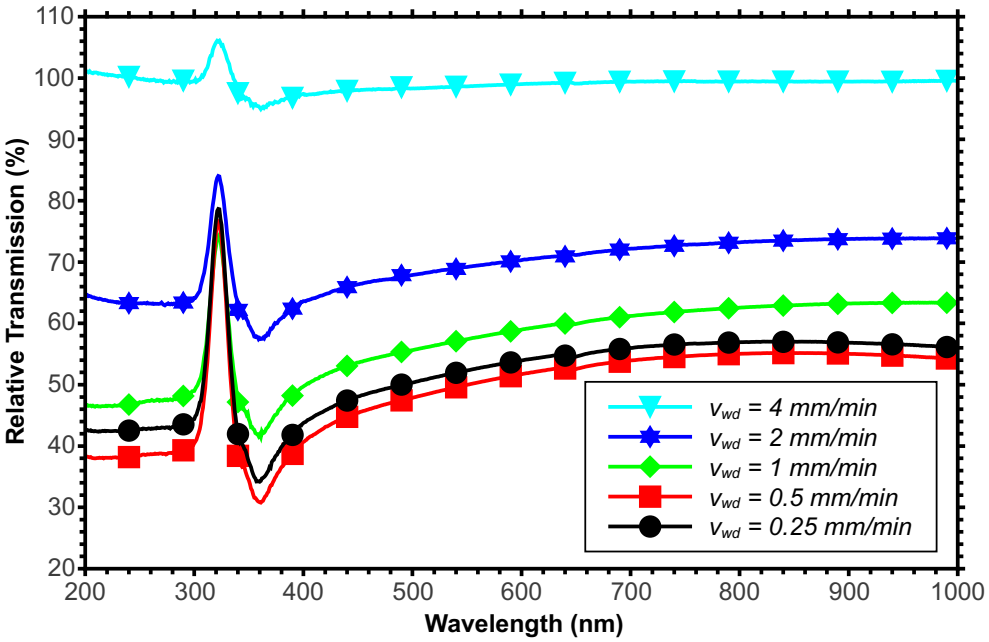

Figure 3.8.: Transmission spectra for AgNW coated cellulose substrates relative to pristine substrates. The substrates were coated with different withdrawal speeds.

maximum at about $\lambda = 320\,\text{nm}$ is due to a light source change of the UV-VIS and can be ignored.

3.2.3. Single cellulose fibers with adsorbed silver nanowires

During the coating process, AgNWs form networks between and around the cellulose fibers of the substrate. Thereby most align themselves along the cellulose fibers. To gain information for the reason of this AgNW-cellulose interactions, IR-spectroscopy was performed. This method can deliver information about chemical interactions by study of molecular vibrational modes. The attenuated total reflectance (ATR) IR measurements were performed on single cellulose fibers. The used ATR-IR measurement setup is described in Section 2.3.5, the sample preparation process in Section 3.1.3.

In Figure 3.9 optical microscopy images of two ATR-IR measured cellulose fibers one pristine, one coated are shown in different magnifications. The AgNWs on its surface are recognizable with high amplification in Figure 3.9(c). For comparison Figure 3.9(d) shows a microscopy surface image of a pristine fiber with the same magnification. The pristine fiber served as AgNW free reference for the ATR-IR

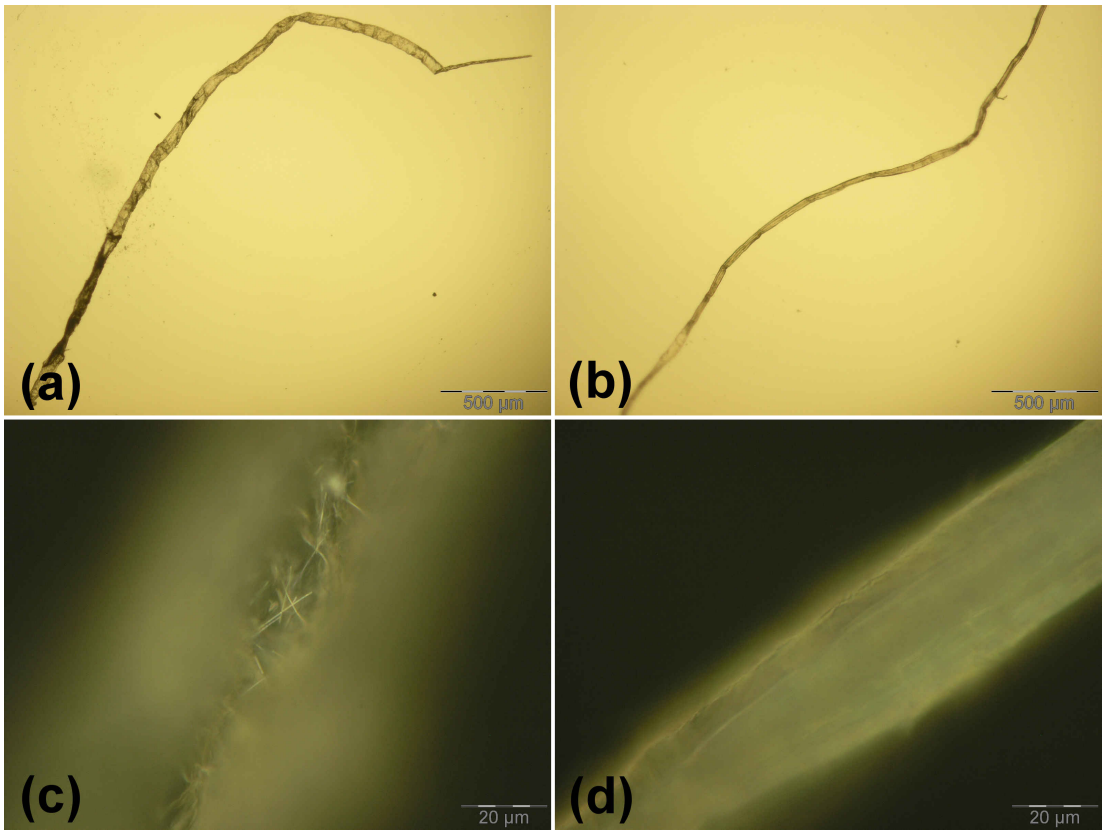

Figure 3.9.: Optical microscopy images of a single pristine cellulose fiber (right) and of a AgNW coated fiber (left). Where the upper images are taken in transmission and the ones below in reflection mode. The scale is embedded in the images.

measurements. This way the detected signals should mostly originate from direct cellulose AgNW interactions.

The ATR-IR measurements were done on two different fibers coated with AgNWs and two pristine fibers, to account for natural variations. The coated fibers are labeled as F1NW ("Fiber 1 Nano Wire") and F4NW, respectively. F7 ("Fiber 7") and F8 ("Fiber 8") are the pristine fibers. In Figure 3.10 ATR-IR spectra are shown. Here the spectrum of a coated fiber, either fiber "F1NW" or fiber "F4NW", was measured and than divided by a reference measurement. The reference measurements are either from another coated or from a pristine fiber like fiber F7 or fiber F8. For clarity the measurements name indicates therefore "sample/reference" for each combination. Spectrum F7/F8 in Figure 3.10 therefor shows the divided spectra of two uncoated fibers. In theory, the ATR-IR

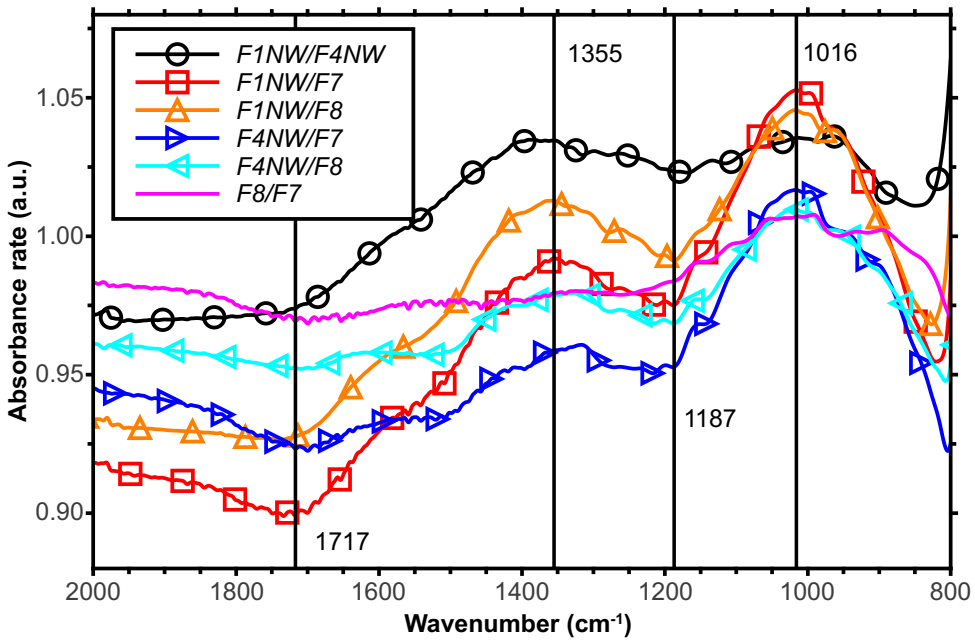

Figure 3.10.: Single Channel Spectra (SCS) relations of different single cellulose fibers. The fibers labeled as F1NW and F4NW are enriched with AgNWs. The ones labeled as F7 and F8 are pristine fibers from the native substrate. The curves are calculated as indicated in the legend.

spectra of F7 and F8 should be alike and the division of these reference spectra should lead to a flat line at 1. In reality, this this is not entirely true. As shown in Figure 3.10 the spectrum is close to 1, but is shifted slightly downwards and shows a subtle peak at about 1016 cm^{-1}. The peak has its origin in C-O stretching of the cellulose molecules. This difference is caused by the uniqueness of each cellulose fiber. This is due to the fact that cellulose fibers are natural species and therefore no two fibers are alike. This fact also has to be considered for the following results.

When comparing two coated fibers, spectrum F1NW/F4NW, a similar effect is seen for the same reason. Theoretically, the spectrum should be a flat line at 1. In praxis, it differs from the expected theoretical behavior. This is shown in Figure 3.10 where two coated fibers are compared in spectrum F1NW/F4NW. There two features are visible. One around 1355 cm^{-1} and the other around 1016 cm^{-1}. The first is assigned to C=O in-plane bending and the latter to C-O stretching of the cellulose molecules. In addition, also the unequal AgNW coverage of the fibers might contribute to the effects.

Table 3.4.: Relative IR-absorption band relations for AgNW enriched and pristine single cellulose fibers. The experimental evaluated values in this table are selected for the relation F1NW/F7. The curve and its values one can find in Figure 3.10.

Feat.	..... Signifies, if the feature is a minimum (min) or a maximum (max) in the spectral relation
λ_{exp}	..... Wavenumber of the bands evaluated from the relation F1NW/F7
Assignment	..... Responsible process. Data from [30] or [31]
Predicted λ	..... Wavenumber given in [30] or [31]

Feat.	λ_{exp} / cm^{-1}	Assignment[30, 31]	Predicted λ /cm^{-1} [30, 31]
min	1717	C=O stretching of carboxyl or lactone groups	1730 -1740
max	1355	C-H bending	1350 - 1355
min	1187	C=O in-plane bending	1205
max	1016	C-O stretching	1015 ‖

In Spectra F1NW/F7, F1NW/F8, F4NW/F7 and F4NW/F8 of Figure 3.10 finally a AgNW coated cellulose fiber has been measured against a pristine cellulose fibers, each time. In these spectra 4 clear features appear between 2000 cm^{-1} and 800 cm^{-1}. The peaks can be assigned to cellulose. They are either caused by C-O or C-H interactions. Thereof, C-O stretching appears at 1016 cm^{-1}, C=O in-plane bending at 1187 cm^{-1}, C-H bending at 1355 cm^{-1} and C=O stretching of carboxyl or lactone groups around 1717 cm^{-1}. They are listed in Table 3.4.
There is no characteristic interaction between the silver nanowires and the cellulose fibers visible in the spectra. Nevertheless, the AgNWs seem to enhance the cellulose signal intensities in IR spectra. This effect was also observed before from Li et al. [31]. The enhanced intensities in the IR spectra were thereby explained by dipole formation at the interface between cellulose and silver particles. The condition of this formation is a very close contact between the cellulose and the silver particles, which is only possible by strong attractive force between them. Also in the mentioned study the origin of the attractive force was not clear. In the present case, therefore strong interactions between the AgNWs and the cellulose fibers are assumed. These strong but unspecific interaction fits to the fact that the AgNWs strongly adhere to the cellulose fibers.

3.3. Summary

To fabricate an electrically conductive cellulose substrate, two attempts were made. One was using reduced graphene oxide (rGO) and one using silver nanowires (AgNWs) as conducting material. The substrates based on rGO showed relatively high resistance over a distance of one cm, in the region of $R > 1\,\mathrm{M}\Omega$. This was caused by island like segregations at the cellulose sheet surface. Additionally the method was found irreproducible and the films inhomogeneous. Therefore, electrically conductive cellulose substrates using rGO as conducting material are not suitable as electrode for organic devices. AgNW based substrates on the other hand, showed desired properties. There, electrically conductive cellulose substrates with a resistance of $R < 100\,\Omega$ and an acceptable transparency ($\sim 70\,\%$) could be produced. These substrates are suitable as a semitransparent electrode for organic semiconductor devices. This is also shown in Section 4 where the fabrication of organic devices on these substrates is presented.
In addition to the electrical and optical properties, also the chemical interactions between the cellulose fibers and the AgNWs were studied. The *IR* spectra indicate strong interactions between the cellulose fibers and the AgNWs. These interactions cause the good adherence of the AgNWs to the cellulose fibers.

4. Organic devices

Based on conductive cellulose fiber networks, organic semiconductor devices were fabricated. The cellulose substrates comprise silver nanowires (AgNWs) as conducting material. The substrate fabrication is described in Section 3. In the following the construction of organic diodes (OD) and organic photovoltaic (OPV) devices is described, respectively.

4.1. Device fabrication

4.1.1. Organic diodes

Electrically conductive paper sheets were produced using AgNWs, as conductive material. Therefore, a AgNW suspension 0.5 $wt\%$ in isopropanol, supplied

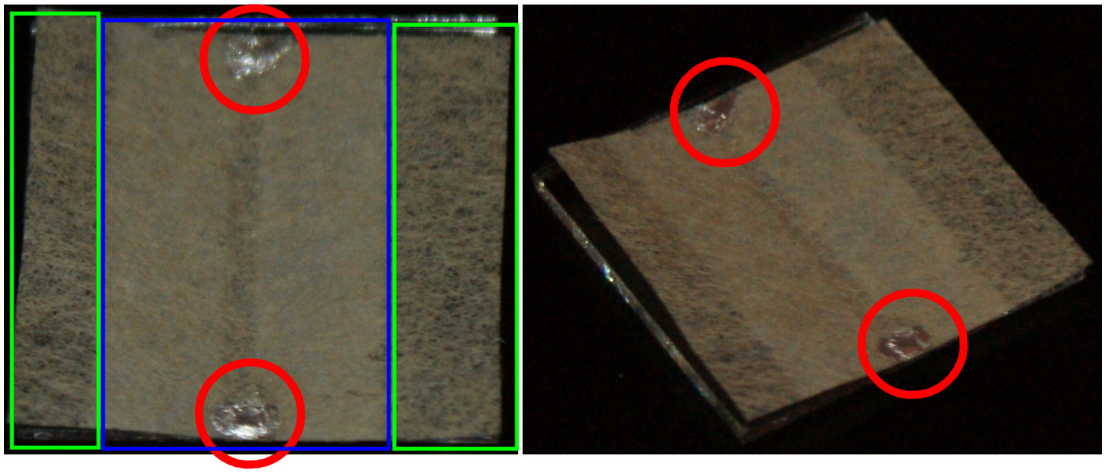

Figure 4.1.: Conductive cellulose substrate with silver dag contact points (red circles). The AgNW network is located on the bottom side of the substrate (blue rectangle). The contact points serve to connect the bottom electrode after active layer deposition. The area marked with the green rectangle does not contain AgNWs.

by Sigma-Aldrich was used. It was further diluted with isopropanol before use. Cellulose substrates were prepared with a size of $(25 \times 40)\,\mathrm{mm}^2$. For material deposition, dip-coating was used. This was accomplished with a SDI Nano DIP ND-0407 dipcoater, described in Section 2.2.1. To avoid vibrations during the dip-process, a Halcyonics active vibration isolation Micro 40 was used. To gain AgNW deposition only on one side of the cellulose, the substrate was folded in half before the coating process. After the dip-coating process the cellulose sheets have been unfolded and dried.
To determine the sample's sheet resistivity, *I-V* measurements were done with a KEITHLEY 2636A SourceMeter® over a distance of about one cm. The measurement settings are described in Section 2.3.1. Additionally transmission spectra in relation to pristine cellulose substrate were taken using a SHIMADZU UV/VIS spectrophotometer. In Section 3.1.2, the fabrication process is described in detail. The conductive cellulose substrate and a glass slide were cut to a size of $(18 \times 18)\,\mathrm{mm}^2$. Contact points with silver dag were set. They were placed on the opposite side to the AgNWs and serve for later contacting. In Figure 4.1 the contact points are shown. The silver dag had to dry for about one hour. To

Table 4.1.: Active material solvent composition for organic diodes.

	Unit	L1000	L1001	L1002
P3HT	mg	103.1	94.4	98.4
o-xylene	mL	2	2	2

improve wettability, the cellulose substrate and the glass slides were treated with O_2 plasma for 90 seconds at maximum power afterwards.
High conductive grade PEDOT:PSS was ultrasonicated. The glass slides with the conductive cellulose substrate on top were placed on the spin coater. The AgNW side was placed face down. PEDOT:PSS was uniformly dispersed on the sample and rotation applied. Following the PEDOT:PSS deposition, the samples were heat-treated under argon flow. All following steps were performed under inert gas conditions in an argon-filled GB. P3HT was dissolved in o-xylene. Three solutions with almost the same P3HT/o-xylene ratio were prepared. In Table 4.1 the exact mixing ratios are provided. The P3HT solution was then heat-treated. Subsequently, the solution was uniformly spread over each sample by drop-casting and left to dry. Eventually, a second layer was deposited. After another drying

Table 4.2.: Organic diode preparation settings:

v_{dip}	..... Dip-in speed into solvent
t_{stop}	..... Waiting time before retraction
v_{wd}	..... Withdrawal speed from solvent
t_{etch}	..... O_2 plasma etching time
p_{etch}	..... Average pressure during the etching process
Flux	..... O_2 flux during the etching process
V_{drop}	..... Liquid volume dropped on to substrate
T_{dry}	..... Drying temperature
t_{dry}	..... Drying time
$\bar{p}_{evap}$	..... Average pressure during the evaporation process
Rate	..... Average evaporation rate
d_{Al}	..... Aluminum thickness

Nr.	Deposite	Methode	P1026	P1028	P1031	P1032	P1036	P1040
1	AgNW dip coating	v_{dip} (μm/s)	500	500	500	500	500	500
		t_{stop} (s)	30	30	30	30	30	30
		v_{wd} (μm/s)	11.33	2	22.64	22.64	11.33	45.48
2	O_2 etching	Power	max	max	max	max	max	max
		t_{etch} (min)	1:30	1:30	1:30	1:30	1:30	1:30
		p_{etch} (mbar)	0.3	0.3	0.3	0.3	0.3	0.3
		Flux	8	8	8	8	8	8
3	PEDOT:PSS 1st Layer spin coating and drying	Ultrasonicated (min)	60	60	25	25	120	120
		U_{spin1} (rpm)	480	480	450	450	450	450
		t_{spin1} (s)	15	15	15	15	15	15
		U_{spin2} (rpm)	650	650	600	600	600	600
		t_{spin2} (s)	15	15	15	15	15	15
		T_{dry1} (℃)	200	200	200	RT	45	45
		t_{dry1} (min)	50	50	80	2	360	360
4	PEDOT:PSS 2nd Layer spin coating and drying	Ultrasonicated (min)	–	–	–	–	60	–
		U_{spin1} (rpm)	–	–	–	450	450	–
		t_{spin1} (s)	–	–	–	15	15	–
		U_{spin2} (rpm)	–	–	–	600	600	–
		t_{spin2} (s)	–	–	–	15	15	–
		T_{dry2} (℃)	–	–	–	200	45-206	45-206
		t_{dry2} (min)	–	–	–	80	225	225
5	P3HT 1st Layer drop casting and drying	Solution heated at $T = 60$℃ for t (h)	L1000 18	L1000 18	L1001 1	L1001 1	L1002 150	L1002 150
		V_{drop1} (μL)	100	100	100	50	50	75
		T_{dry4} (℃)	room temperature					
		t_{dry4} (h)	3.5	3.5	4.5	4.5	7	7
6	P3HT 2nd Layer drop casting and drying	Solution heated at $T = 60$℃ for t (h)	L1000 22	L1000 22	L1001 5.5	L1001 5.5	L1002 157	L1002 157
		V_{drop2} (μL)	200	200	100	100	75	75
		T_{dry5} (℃)	room temperature					
		t_{dry5} (h)	19.5	19.5	150	150	24	24
7	Aluminum Evaporation	$\bar{p}_{evap}$ (10^{-5} mbar)	1.3	1.3	1.1	1.1	1.5	1.5
		Av. Rate (nm/min)	6	6	5	5	40	40
		d_{Al} (nm)	90	90	100	100	100	100

period the samples were transferred to a thermal evaporator. There, aluminum was evaporated as top electrode on the devices. In Table 4.2 detailed information on every fabrication process step are given.
To quantify the fabricated devices, *I-V* measurements were done. The measurement process is described in Section 2.3.1. In Section 4.2.1 one can find the results.

4.1.2. Organic photovoltaic cells

Electrically conductive paper sheets were produced using silver nanowires (AgNWs), as conductive material. Therefore, a AgNW suspension $0.5\,wt\%$ in isopropanol, supplied by Sigma-Aldrich was used. It was further diluted with isopropanol before use. Cellulose substrates were prepared with a size of $(25x40)\,\mathrm{mm}^2$. For material deposition, dip-coating was used. This was accomplished with a SDI Nano DIP ND-0407 dip-coater, described in Section 2.2.1. To avoid vibrations during the dip process, a Halcyonics active vibration isolation Micro 40 was used. To gain AgNW deposition only on one side of the cellulose, the substrate was folded in half before the coating process. After the dip-coating process the cellulose sheets have been unfolded and dried.
To determine the sample's sheet resistivity, *I-V* measurements were done with a KEITHLEY 2636A SourceMeter® over a distance of about one cm. The measurement settings are described in Section 2.3.1. Additionally transmission spectra in relation to pristine cellulose substrate were taken using a SHIMADZU UV/VIS spectrophotometer.
The conductive cellulose substrate and a microscopy slide were cut to a size of $(18x18)\,\mathrm{mm}^2$. On the opposite side to the AgNWs, contact points with silver dag

Table 4.3.: Detailed record of the solution composition

	Unit	L1301	L1302
P3HT	mg	55	50
$PC_{60}BM$	mg	110	101
o-xylene	mL	3	–
Chlorobenzene	mL	–	3

were set on the cellulose substrate. These are necessary to connect the bottom electrode during the *I-V* characterization of the OPVs. The silver dag had to

Table 4.4.: Sample preparation settings, where Monopol X - Cellulose was used as Substrate.

v_{dip} ..... Dip-in speed into solvent
t_{stop} ..... Waiting time before retraction
v_{wd} ..... Withdrawal speed from solvent
t_{etch} ..... O_2 plasma etching time
p_{etch} ..... Average pressure during the etching process
Flux ..... O_2 flux during the etching process
V_{drop} ..... Liquid volume dropped on to Substrate
T_{dry1} ..... Drying temperature
t_{dry1} ..... Drying time
$\bar{p}_{evap}$ ..... Average pressure during the evaporation process
Rate ..... Average evaporation rate
d_{Al} ..... Aluminum thickness

Nr.	Deposite	Methode	P1314	P1335
1	AgNW dip coating	v_{dip} (μm/s)	500	500
		t_{stop} (s)	30	30
		v_{wd} (μm/s)	33.33	33.33
2	O_2 etching	Power	max	max
		t_{etch} (min:s)	9:30	9:30
		p_{etch} (mbar)	0.3	0.3
		Flux	8	8
3	PEDOT:PSS drop coating	Ultra Sonic treatment for 30 min		
		V_{drop1} (μL)	100	100
4	Heat treatment	T_{dry1} (℃)	125	70
		t_{dry1} (min)	30	25
		T_{dry2} (℃)	200	150
		t_{dry2} (min)	30	20
		T_{dry3} (℃)	-	200
		t_{dry3} (min)	-	15
5	Active Layer drop casting	Solution	L1301	L1302
		heat treated for $\sim$ 3 h at $T \approx$ 70℃		
		V_{drop2} (μL)	70	70
		T_{dry4} (℃)	70	70
		t_{dry4} (min)	10	10
		V_{drop3} (μL)	100	100
		T_{dry5} (℃)	70	70
		t_{dry5} (min)	15	15
		V_{drop4} (μL)	100	100
		T_{dry6} (℃)	70	70
		t_{dry6} (min)	20	20
6	Aluminum Evaporation	$\bar{p}_{evap}$ (10^{-6} mbar)	1.2	1.2
		Av. Rate (nm/min)	8	8
		d_{Al} (nm)	100	100

dry for about one hour after deposition. In Figure 4.1 some cellulose sheets with such contact points are depict. Before coating with the organic follow-on layers, the substrates and the glass slides were treated with O_2 plasma to improve wettability.
High conductive grade PEDOT:PSS was ultrasonic treated. The cellulose was applied with the conductive side down on the glass slide and PEDOT:PSS was uniformly dispersed on the sample. Afterwards the samples were heat treated under Ar flow and transfered to the glove box.
Under Ar atmosphere P3HT mixed with $PC_{60}BM$ was diluted in o-Xylene and chlorobenzene, respectively. The solution was heat treated for several hours. For concentrations see Table 4.3.
The two solutions were uniformly spread on to the samples by drop-casting and left to dry. Subsequently, a second and eventually a third organic semiconducting layer was applied. After another drying period, Al was evaporated as top electrode of the device. Further informations about the device fabrication can be found in Table 4.4.
To evaluate the fabricated organic photovoltaic cells, *I-V* measurements under Ar atmosphere were accomplished as described in Section 2.3.1. The results can be found in Section 2.3.1.

4.2. Device characterization

4.2.1. Conductive cellulose based organic diodes

As described in Section 4.1.1 organic diodes were fabricated on conductive cellulose substrate. P3HT was used as photo-active and PEDOT:PSS as hole blocking layer. As top electrode Al was evaporated. In Figure 4.2 a schematic illustration of the diode architecture is illustrated. In Figure 4.3 an image of a fabricated diode is shown. There, six independent OPV pixels are visible. They contain of an active area and a connecting region. The active area is located above the AgNWs and has a size of around $(3 \times 3)\,\mathrm{mm}^2$. The connecting region lies above the AgNW free region of the device. This is necessary to prevent short circuits caused by the contact pressure when connecting them with the micro-probes.
To evaluate the diodes properties, *J-V* curves were recorded. The current den-

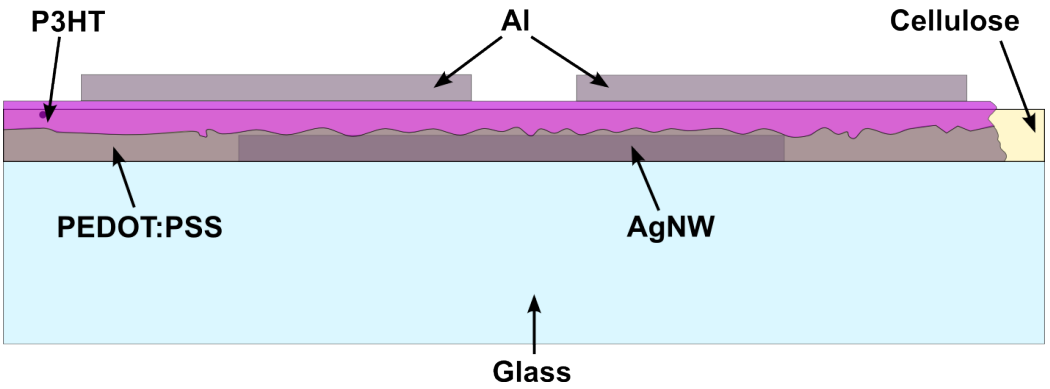

Figure 4.2.: Schematic illustration of the diode architecture.

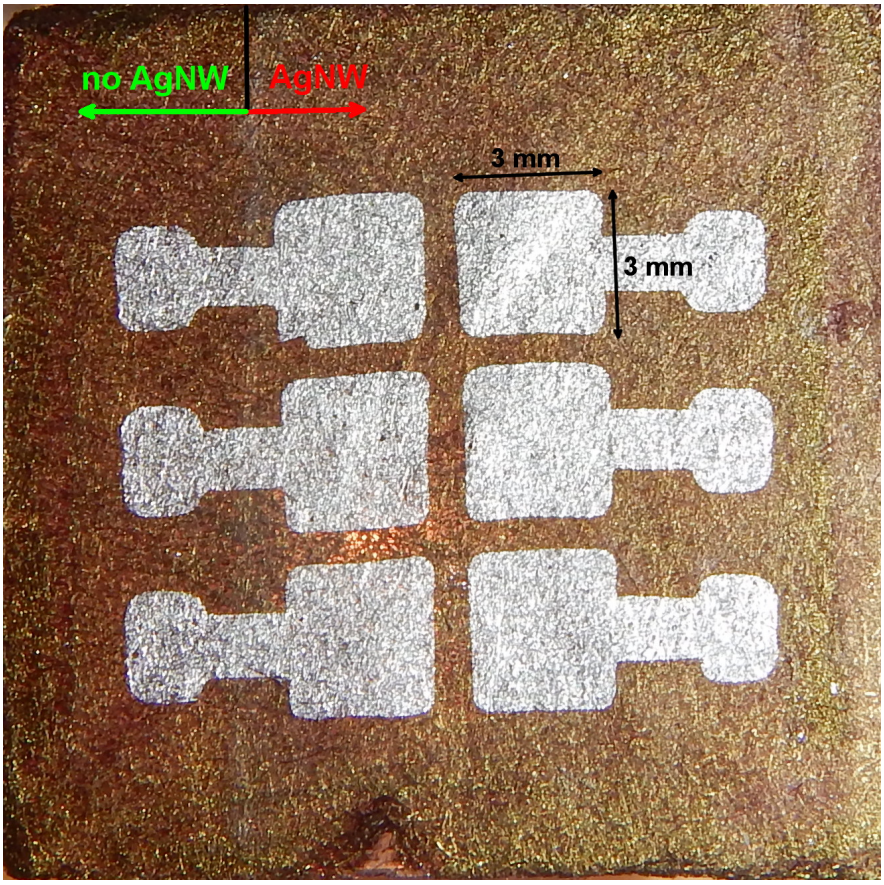

Figure 4.3.: Image of a fabricated device.

sity was calculated for a nominal pixel size of $(3 \times 3)\,\mathrm{mm}^2$. In Section 2.3.1 the measurement procedure is described. The measurements were done in both directions: forward sweep mode - scan from negative voltage values to positive; and reverse sweep mode - scan from positive to negative voltage values. The J-V

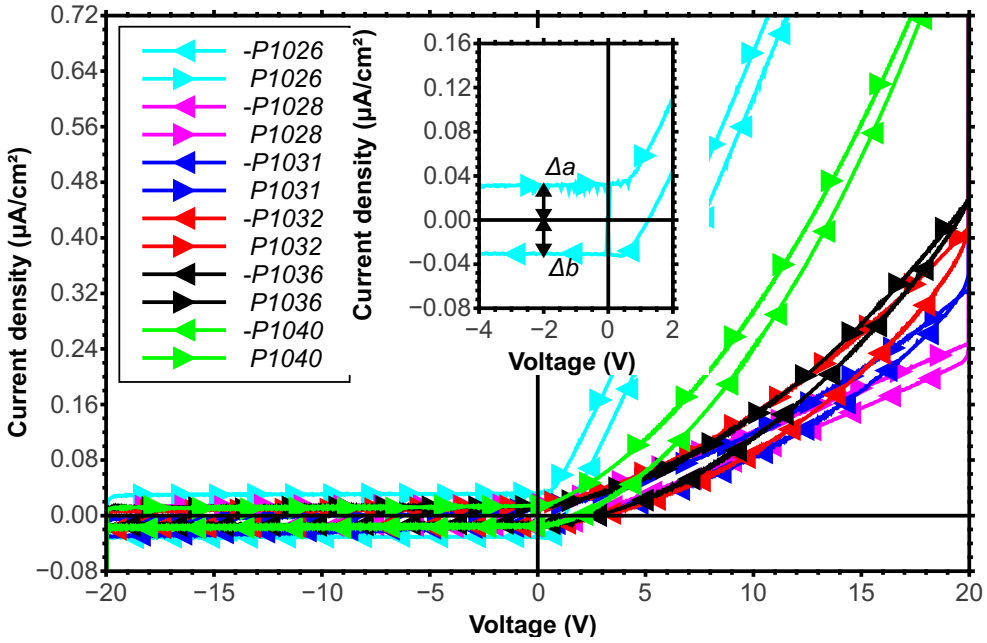

Figure 4.4.: Current density of different organic diodes measured in forward and reverse sweep, respectively. The measurements were performed under ambient light. The "-" signifies reverse sweep mode.

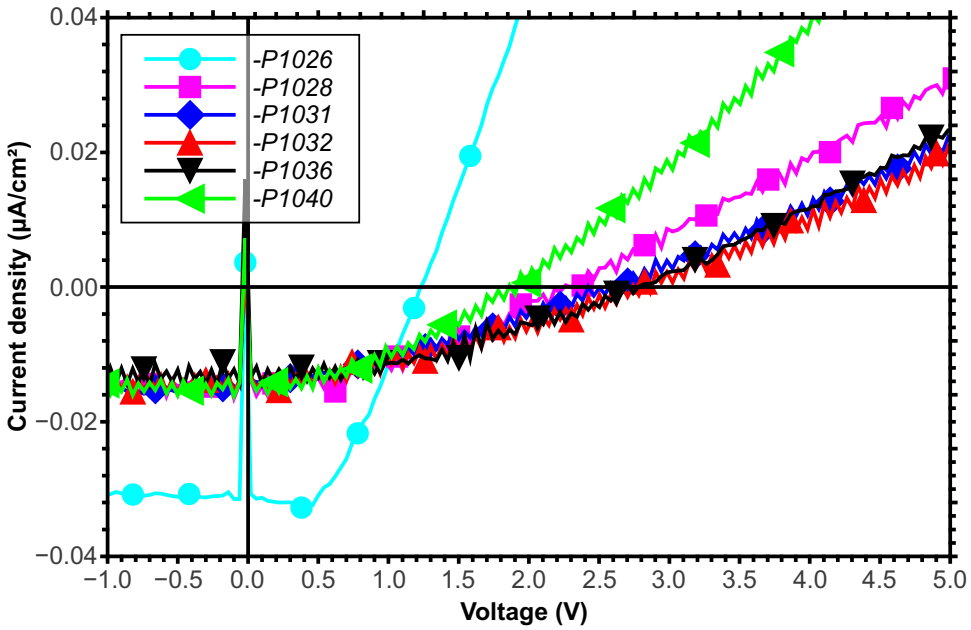

Figure 4.5.: Current density of different organic diodes measured in reverse bias. The measurements were performed under ambient light. At zero Voltage measurement artifacts appear. These are ascribed to the KEITHLEY measurement setup and can be ignored.

curves of different organic diodes are illustrated in Figure 4.4. The "-"sign labels reverse sweep measurements.
By examining the curves, a hysteresis is visible between the forward and reverse-biased measurements. The inset in Figure 4.4 shows the J-V curve of a single diode in detail. In the negative voltage range the curve is symmetrically shifted around the zero current line. The shifts are marked with $\triangle a$ and $\triangle b$, were $\triangle a \approx \triangle b$. This symmetrical shift appears in all measurements. Capacitive or electrostatic effects seem to be a reasonable explanation for this effect. In literature [32] the effect is also assigned to capacitive effects caused by a too fast scanning interval.
Nevertheless, the characteristic clearly shows diode behavior. For a better overview, solely the reverse sweep measurements are shown in Figure 4.5. The fabricated diodes were produced with varying active layer thicknesses, controlled by the amount drop casted. Therefore the P3HT layer thickness decreases from device P1026 to device P1040. By observing the J-V curves in Figure 4.5 it is obvious that the two curves -P1026 and -P1040, show the steepest current increase, despite the fact that they have very different active layer thickness. Therefore the active layer thickness seems not to have strong impact on the diode characteristics. However, a thicker active layer leads to a higher number of functioning devices. This is caused by a decrease of short circuits between the device top and bottom electrodes. Because of the current shift, it is not possible to determine the absolute dark current of the diodes. Besides, the measurement was performed under ambient light. Anyhow, it is impressive that the breakdown voltage of the devices lies beyond $-20\,\mathrm{V}$. Additionally the leakage current does not increase significantly with increasing reverse voltage as is shown in Figure 4.4. By observing the curve -P1026 in Figure 4.5 the set on voltage is estimated between 0.5 and 0.7 V. This is a typical value for organic diodes based on P3HT [33]

4.2.2. Conductive cellulose based organic photovoltaic cells

Organic photovoltaic (OPV) cells were produced as described in Section 4.1.2. Conductive cellulose fiber networks were used as substrate. PEDOT:PSS served as hole blocking layer and a blend of P3HT and $PC_{60}BM$ were used as active materials. Silver dag was used to contact the bottom electrode as described above (Figure 4.1). Al was evaporated as top electrode. In Figure 4.6 a schematic il-

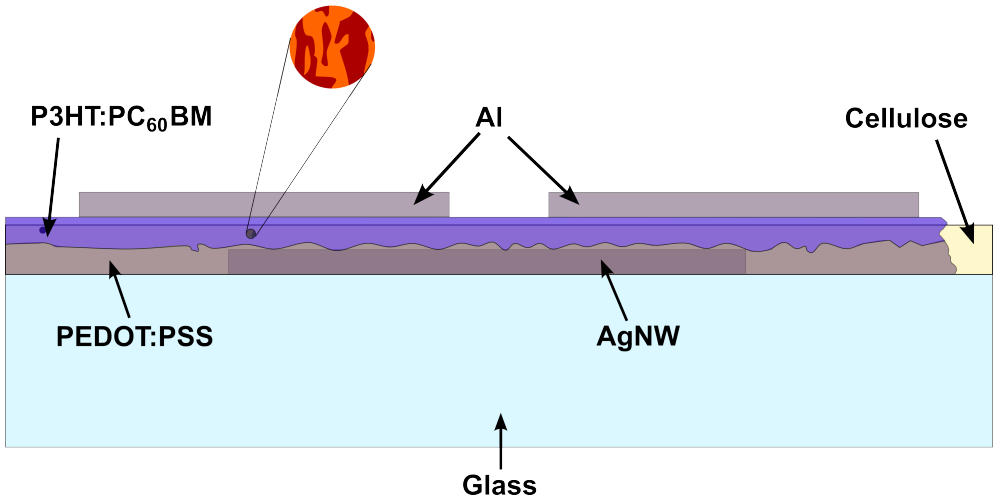

Figure 4.6.: Schematic illustration of the OPV architecture.

lustration of the OPV architecture is shown. Optically, an OPV devices do not differ from an organic diode as depict in Figure 4.3.

I-V measurements were done under inert gas condition inside the GB. Both, measurements under direct illumination and with indirect illumination were accomplished. For direct illumination an OSRAM® LED light and for indirect illumination UV-filtered yellow ambient light was used, respectively. Forward and reverse sweep measurements were executed during one measurement cycle. The current density was calculated for a nominal pixel size of $(3 \times 3)\,\mathrm{mm}^2$. In Section 2.3.1 the measurement setup is described in detail.

The photovoltaic characteristic of device P1335 is shown in Figure 4.7 in linear and Figure 4.8 in semi-log scale. For this device chlorobenzene was used for the active layer deposition. The black curve was recorded under indirect ambient light illumination, whereas the red curve was measured under direct light illumination. Both curves show considerable photo-activity. Nevertheless, an increase of the photo-current is especially visible under direct illumination. In ambient light measurements, the device showed a short circuit current (J_{SC}) of $0.05\,\mu\mathrm{A/cm}^2$ and an open circuit voltage (V_{OC}) of 0.04 V with a fill factor (FF) of 27 %. Under direct light illumination the current increases to $J_{OC} = 0.12\,\mu\mathrm{A/cm}^2$ and the voltage to $V_{OC} = 0.05\,\mathrm{V}$. The FF reaches 30 %.

In Figure 4.9 and Figure 4.10 *J-V* curves of device P1314 is shown in linear scale and semi-log scale, respectively. For this sample o-xylene was used as solvent for

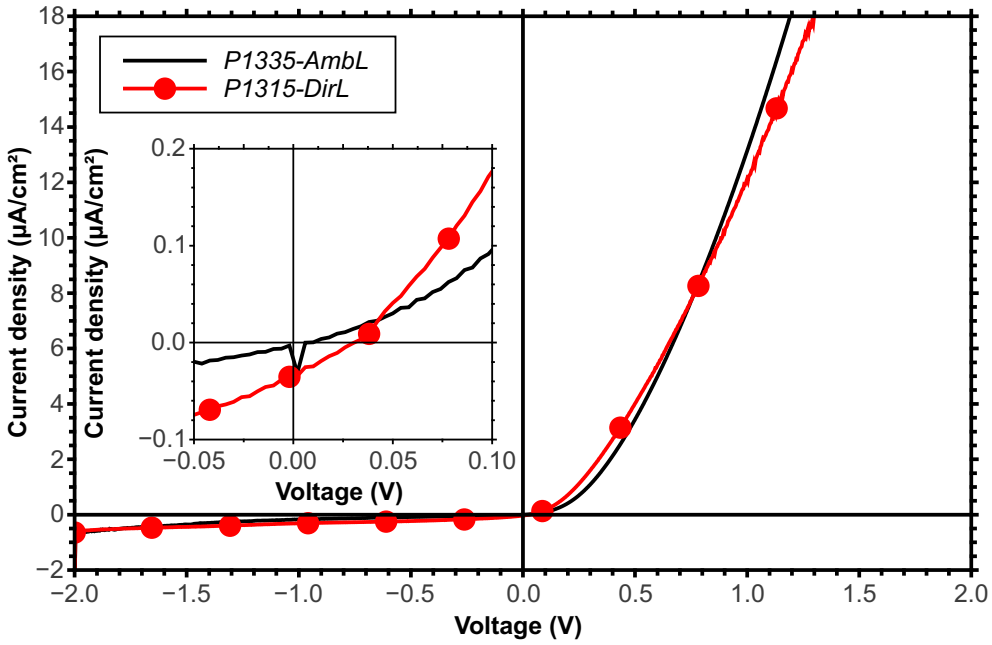

Figure 4.7.: J-V characteristics of device P1335. The active layer was deposited from chlorobenzene. The measurements were done with ambient light (-AmbL) and with direct LED illumination (-DirL).

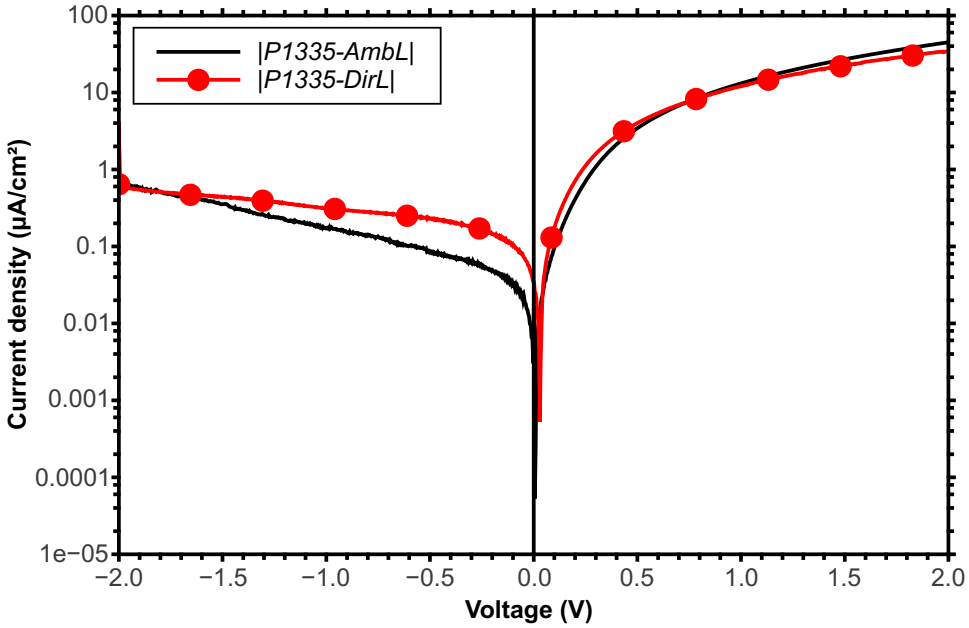

Figure 4.8.: J-V characteristics of device P1335 on a semi-log scale. The active layer was deposited from chlorobenzene. The measurements were done with ambient light (-AmbL) and with direct LED illumination (-DirL).

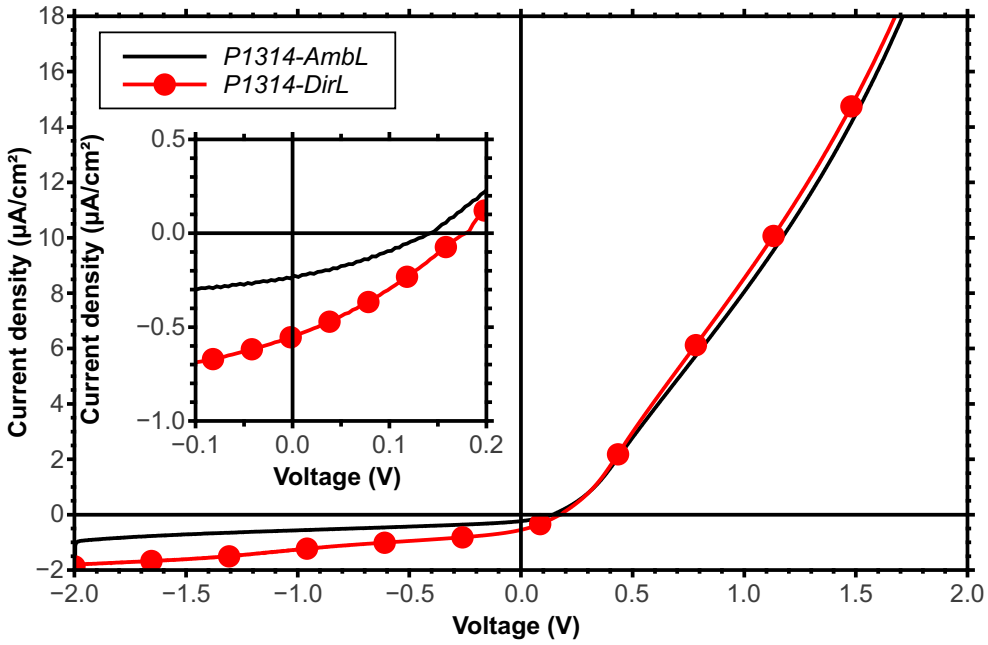

Figure 4.9.: J-V characteristics of device P1314. The active layer was deposited from chlorobenzene. The measurements were done with ambient light (-AmbL) and with direct LED illumination (-DirL).

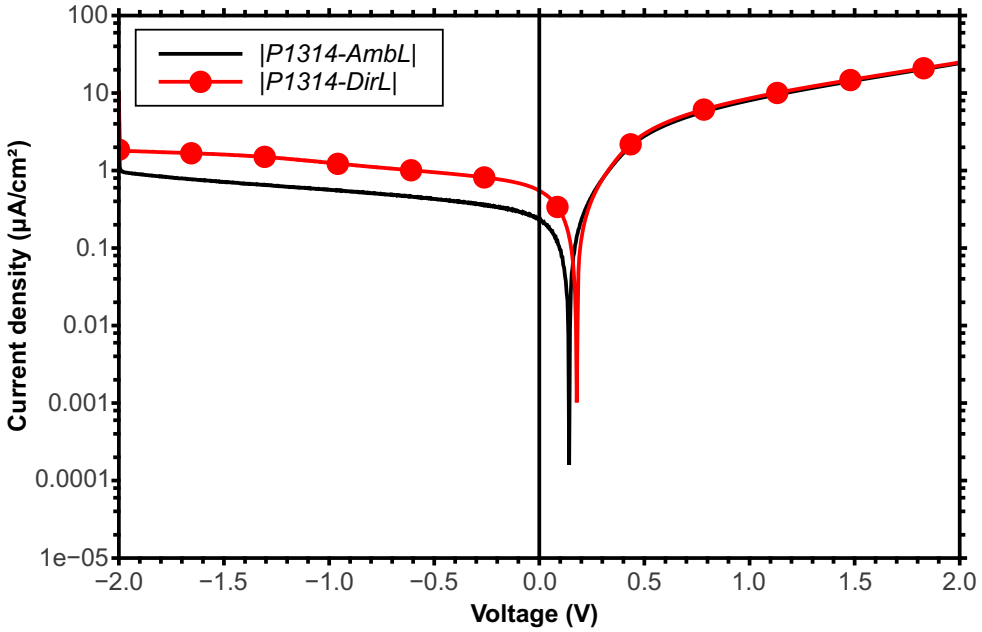

Figure 4.10.: J-V characteristics of device P1314 on a semi-log scale. The active layer was deposited from chlorobenzene. The measurements were done with ambient light (-AmbL) and with direct LED illumination (-DirL).

the active material solution. As above, the black curve was recorded under indirect ambient light illumination, whereas the red curve was measured under direct light illumination. For ambient light the device showed a J_{SC} of $0.23\,\mu A/cm^2$ and an V_{OC} of $0.14\,V$ with a FF of $34\,\%$. Under direct light illumination the current increases to $J_{OC} = 0.55\,\mu A/cm^2$ and the voltage to $V_{OC} = 0.18\,V$, whereas FF decreased to $30\,\%$.

A light intensity dependency of the photo-current is clearly revealed when com-

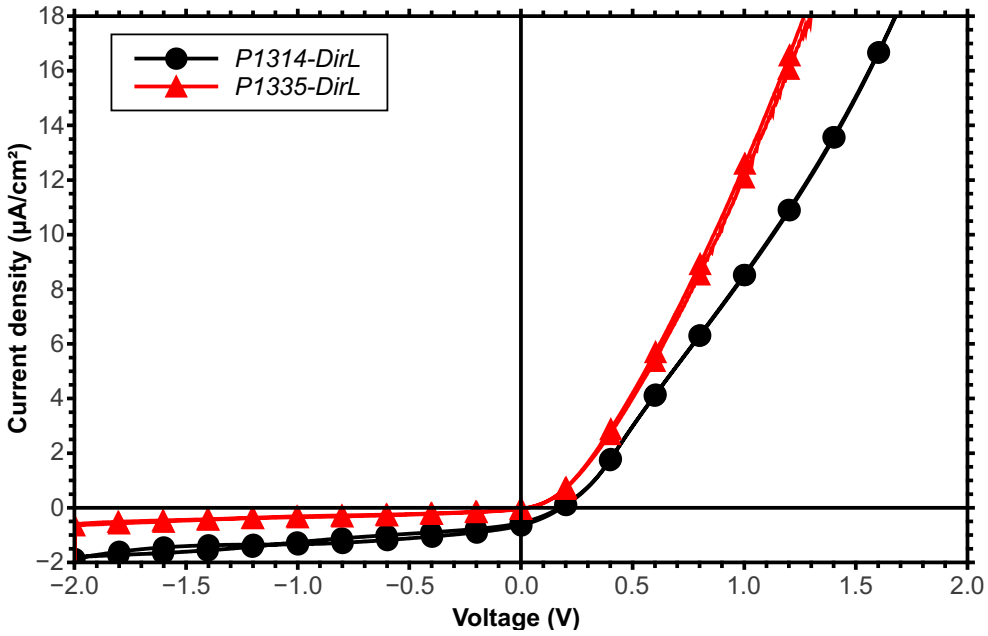

Figure 4.11.: Current density of different OPV cells measured in forward and reverse bias, respectively. The measurements were done with ambient light and with direct

paring the stray light measurements with the measurements under direct illumination, for both samples. Both devices show a shift of J_{SC} and V_{OC}, as known for traditional planar devices with ITO as transparent anode [34, 35]. At the used illumination intensities the devices show no sign of imbalanced charge transport or any kind of blocking behavior. This would reflect in a S-kink deteriorated J-V curve. Anyhow, the S-kink usually does not appear for low intensity illumination measurements [36]. Due to comparison of the two devices the characteristics show a significant enhancement of performance by changing the active layer solvent from chlorobenzene to o-xylene. In Figure 4.11, again the measurements under direct illumination of the two samples are shown in direct comparison.

Since reports on planar devices in literature show similar device performance for according films derived from o-xylene and chlorobenzene this insight was unexpected [37]. A possible explanation for this could be the difference in interactions between the solvents and the cellulose fibers. This is supported by the observation that chlorobenzene is absorbed in less than one second by the cellulose, while it takes a few seconds for o-xylene. The difference in solution absorption by the cellulose fibers could influence the film formation of the active material an the cellulose fiber surface. It is a widely known fact that phase-separation in P3HT:PC_{60}BM is strongly influenced by substrate and solvent interaction. This phase-separation plays an important role in device performance of organic solar cells. It is suggested that the apparent difference in device performance between o-xylene and the chlorobenzene deposited sample can be explained with that.

4.3. Summary

Functional organic devices have been fabricated on conductive cellulose fiber networks. Thereby silver nanowires were absorbed to the surface of unrefined kraft pulp fiber sheets. They were used as semitransparent electrode (Anode). *PEDOT:PSS* was coated on the anode as electron blocking layer. P3HT for diodes and a blend of P3HT:PC_{60}BM for OPVs were used as active layer, respectively. The devices were finished with an evaporated metal (Al) cathode.
The fabricated organic diodes showed impressive breakdown voltages above $-20\,\mathrm{V}$. Additionally, the diodes show no significant increase of leakage current. Their estimated set on voltage lied between 0.5 and 0.7 V, which is a reasonable value for P3HT based organic diodes.
The OPV devices were measured under ambient light illumination and under direct illumination, using a LED light as source. Due to the scattering effect of the cellulose the devices showed photo-activity even under low indirect illumination. Nevertheless, an increase in photo-current could be seen under direct illumination. There the devices showed quite decent performance. Fill factor up to 35 % could be achieved. Under direct light illumination using a LED light the current reached values up to $J_{OC} = 0.55\,\mu\mathrm{A/cm^2}$ and an open circuit voltage of $V_{OC} = 0.18\,\mathrm{V}$. Further on, a significant difference in performance was found depending on the solvent used for active layer deposition. This is associated with

the different absorption behavior between the solvents and the cellulose.
In literature [28] P3HT:$PC_{60}BM$ OPVs using ITO and AgNWs on Glass as anode were compared, respectively. Performing measurements under AM1.5G illumination they observed FF of 61 % for the ITO cell and 52 % for the AgNW based cell with $V_{OC,ITO} = 0.58\,\mathrm{V}$ and $V_{OC,AgNW} = 0.52\,\mathrm{V}$, $J_{SC,AgNW} = 9.0\,\mathrm{mA/cm^2}$ and $\mathrm{J}_{SC,ITO} = 9.3\,\mathrm{mA/cm^2}$. These values are significantly higher than the here presented values. But considering the low light illumination used and that the devices were not optimized yet the results are still stunning. However, it has been shown that conductive cellulose fiber networks can be used as semitransparent electrode for organic devices like diodes and OPVs.

5. Conclusion and outlook

In this work, the fabrication of organic devices based on a conducting cellulose fiber network is described. At first electrically conductive cellulose fiber networks have been fabricated. Therefore unrefined and unbleached kraft pulp fiber sheets were used as cellulose substrate. Silver nanowires (AgNWs) were used as conducting material. The AgNWs have been absorbed on the cellulose surface by simply dip-coating. Thereby, electrically conductive cellulose substrates with a resistance $R < 100\,\Omega$ and an acceptable relative transparency ($\sim 70\,\%$) could be produced. This makes these substrates suitable as a semitransparent electrode for organic semiconductor devices, as was shown in Section 4. There, the fabrication process of organic diodes and organic photovoltaic (OPVs) devices is described in detail. Additionally, their electrical characteristics are discussed in this section. For organic devices PEDOT:PSS was coated on the anode (conductive cellulose fiber network) as electron blocking layer. P3HT for diodes and a blend of P3HT:$PC_{60}BM$ for OPVs were used as active layer, respectively. The devices were finalized with an evaporated metal (Al) cathode.

The fabricated organic diodes showed impressive breakdown voltages above $-20\,\mathrm{V}$. Additionally, no significant increase of leakage current could be determined. Their estimated set-on voltage was located between 0.5 and 0.7 V, which is a reasonable value for P3HT based organic diodes.

The OPV devices were measured in an inert gas environment under ambient light illumination and under direct illumination, using a LED light as source. Due to the scattering effect of the cellulose the devices showed photo-activity even under low indirect illumination. Nevertheless, an increase in photo-current could be seen under direct illumination. There the devices showed quite decent performance. Fill factor up to 35 % could be achieved. Further on, a significant difference in performance was found depending on the solvent used for active layer deposition. This is associated with the different absorption behavior between the solvents and

the cellulose. However, it could be shown that electrically conducting cellulose fibers are a possible material for semitransparent electrodes in organic semiconductor devices.

Like mentioned above the OPV characterization during this work was accomplished under indirect ambient and under direct illumination using a LED light, respectively. For a better qualitative rating and for comparison with other devices, dark current and solar simulator measurements need to be done in future research studies. Therefore, it is also necessary to improve the electrically contacting between the devices and the measurement equipment. Additional research needs to be done to optimize layer deposition, layer thicknesses and layer composition.

Bibliography

[1] Daniel Tobjörk and Ronald Österbacka. "Paper Electronics." In: *Advanced Materials* 23.17 (2011), pp. 1935–1961. ISSN: 1521-4095. DOI: 10.1002/adma.201004692. URL: http://dx.doi.org/10.1002/adma.201004692.

[2] R. Martins, I. Ferreira, and E. Fortunato. "Electronics with and on paper." In: *physica status solidi (RRL) – Rapid Research Letters* 5.9 (2011), pp. 332–335. ISSN: 1862-6270. DOI: 10.1002/pssr.201105247. URL: http://dx.doi.org/10.1002/pssr.201105247.

[3] Zhe Weng et al. "Graphene–Cellulose Paper Flexible Supercapacitors." In: *Advanced Energy Materials* 1.5 (2011), pp. 917–922. ISSN: 1614-6840. DOI: 10.1002/aenm.201100312. URL: http://dx.doi.org/10.1002/aenm.201100312.

[4] Ute Zschieschang et al. "Organic Electronics on Banknotes." In: *Advanced Materials* 23.5 (2011), pp. 654–658. ISSN: 1521-4095. DOI: 10.1002/adma.201003374. URL: http://dx.doi.org/10.1002/adma.201003374.

[5] Jin-Woo Han et al. "A carbon nanotube based ammonia sensor on cellulose paper." In: *RSC Adv.* 4 (2 2014), pp. 549–553. DOI: 10.1039/C3RA46347H. URL: http://dx.doi.org/10.1039/C3RA46347H.

[6] Xinyi Chen et al. "Role of mesoporosity in cellulose fibers for paper-based fast electrochemical energy storage." In: *J. Mater. Chem. A* 1 (28 2013), pp. 8201–8208. DOI: 10.1039/C3TA10972K. URL: http://dx.doi.org/10.1039/C3TA10972K.

[7] Georgia Tech Robert C. Williams Paper Museum. *The Invention of Paper*. URL: http://www.ipst.gatech.edu/amp/collection/museum_invention_paper.htm (visited on 05/15/2014).

[8] Wikipedia. *Friedrich Gottlob Keller*. URL: http://en.wikipedia.org/wiki/Friedrich_Gottlob_Keller (visited on 05/15/2014).

[9] Paper Industry. *Understanding the Kraft Process in Paper Production*. URL: http://www.paperindustry.com/kraft-process.asp (visited on 05/27/2014).

[10] Austropapier. *The Anual Report of the Austrian Paper Industry 2013*. Tech. rep. Austropapier, 2013. URL: http://www.austropapier.at/fileadmin/Austropapier/Dokumente/JB_2013/xx__Jahresbericht_2013_gesPDF__v2_.pdf (visited on 05/27/2014).

[11] Herbert Sixta. "Introduction." In: *Handbook of Pulp*. Wiley-VCH Verlag GmbH, 2008, pp. 2–19. ISBN: 9783527619887. DOI: 10.1002/9783527619887.ch1. URL: http://dx.doi.org/10.1002/9783527619887.ch1.

[12] Oleksandr V. Mikhnenko. "Singlet and Triplet Excitons in Organic Semiconductors." PhD thesis. University of Groningen, the Netherlands, 2012. ISBN: 978-90-367-5201-5.

[13] The Inkscape Team. *Inkscape 0.48 - Vector Graphics Editor*. Free Software Foundation, Inc. Boston, USA, 2014. URL: www.inkscape.org.

[14] Peter Vollhardt and Neil Schore. *Organic Chemistry: Structure and Function*. 6th ed. Clancy Marshal, 2011.

[15] Christopher R. McNeill and Neil C. Greenham. "Conjugated-Polymer Blends for Optoelectronics." In: *Advanced Materials* 21.38-39 (2009), pp. 3840–3850. ISSN: 1521-4095. DOI: 10.1002/adma.200900783. URL: http://dx.doi.org/10.1002/adma.200900783.

[16] Valentin Dan Mihailetchi. "Device Physics of Organic Bulk Heterojunction Solar Cells." PhD thesis. Rijksuniversiteit Groningen, the Netherlands, 2005. ISBN: 90-367-2393-0.

[17] N. S. Sariciftci et al. "Photoinduced Electron Transfer from a Conducting Polymer to Buckminsterfullerene." In: *Science* 258.5087 (1992), pp. 1474–1476. DOI: 10.1126/science.258.5087.1474. eprint: http://www.sciencemag.org/content/258/5087/1474.full.pdf. URL: http://www.sciencemag.org/content/258/5087/1474.abstract.

[18] Christoph J Brabec et al. "Tracing photoinduced electron transfer process in conjugated polymer/fullerene bulk heterojunctions in real time." In: *Chemical Physics Letters* 340.3–4 (2001), pp. 232 –236. ISSN: 0009-2614. DOI: http://dx.doi.org/10.1016/S0009-2614(01)00431-6. URL: http://www.sciencedirect.com/science/article/pii/S0009261401004316.

[19] Charles L. Braun. "Electric field assisted dissociation of charge transfer states as a mechanism of photocarrier production." In: *The Journal of Chemical Physics* 80.9 (1984), pp. 4157–4161. DOI: http://dx.doi.org/10.1063/1.447243. URL: http://scitation.aip.org/content/aip/journal/jcp/80/9/10.1063/1.447243.

[20] V. D. Mihailetchi et al. "Cathode dependence of the open-circuit voltage of polymer-fullerene bulk heterojunction solar cells." In: *Journal of Applied Physics* 94.10 (2003), pp. 6849–6854. DOI: http://dx.doi.org/10.1063/1.1620683. URL: http://scitation.aip.org/content/aip/journal/jap/94/10/10.1063/1.1620683.

[21] Royal Society of Chemistry. *Drop Coating*. URL: http://www.rsc.org/publishing/journals/prospect/ontology.asp?id=CMO:0002163&MSID=b9nr00004f (visited on 02/18/2014).

[22] Plank Harald. *Focused Ion Beam Microscopy*. Institute für Elektronenmikroskopie und Nanoanalytik. 2011. URL: www.felmi-zfe.at.

[23] S. Amelinckx et al. "Scanning Electron Microscopy." In: *Handbook of Microscopy*. Wiley-VCH Verlag GmbH, 2008, pp. 539–561. ISBN: 9783527620524. DOI: 10.1002/9783527620524.ch1. URL: http://dx.doi.org/10.1002/9783527620524.ch1.

[24] Mario Djak. "Investigation of cellulose-hemicellulose films on Si/SiO2 substrates by means of Polarization Modulation Fourier Transform Infrared Spectroscopy." Masters Thesis. Graz University of Technology, Oct. 2011.

[25] Eduard Gilli. "IR spectroscopic investigations on the chemical surface properties of cellulose fibers." Masters Thesis. Graz University of Technology, Oct. 2008.

[26] Fernández-Merino et al. “Vitamin C Is an Ideal Substitute for Hydrazine in the Reduction of Graphene Oxide Suspensions.” In: *J. Phys. Chem. C,* 114.14 (2010), pp. 6426–6432.

[27] A. Mosca Conte et al. “Visual degradation in Leonardo da Vinci's iconic self-portrait: A nanoscale study.” In: *Applied Physics Letters* 104.22 (2014), pp. –. DOI: http://dx.doi.org/10.1063/1.4879838. URL: http://scitation.aip.org/content/aip/journal/apl/104/22/10.1063/1.4879838.

[28] Johannes Krantz et al. “Solution-Processed Metallic Nanowire Electrodes as Indium Tin Oxide Replacement for Thin-Film Solar Cells.” In: *Advanced Functional Materials* 21.24 (2011), pp. 4784–4787. ISSN: 1616-3028. DOI: 10.1002/adfm.201100457. URL: http://dx.doi.org/10.1002/adfm.201100457.

[29] A. Graff et al. “Silver nanowires.” English. In: *The European Physical Journal D - Atomic, Molecular, Optical and Plasma Physics* 34.1-3 (2005), pp. 263–269. ISSN: 1434-6060. DOI: 10.1140/epjd/e2005-00108-7. URL: http://dx.doi.org/10.1140/epjd/e2005-00108-7.

[30] D. Klemm et al. “Analytical Methods in Cellulose Chemistry: Section 3.3.” In: *Comprehensive Cellulose Chemistry*. Wiley-VCH Verlag GmbH and Co. KGaA, 2004, pp. 181–195. ISBN: 9783527601929. DOI: 10.1002/3527601929.ch3c. URL: http://dx.doi.org/10.1002/3527601929.ch3c.

[31] Shu-Ming Li et al. “Cellulose-silver nanocomposites: Microwave-assisted synthesis, characterization, their thermal stability, and antimicrobial property.” In: *Carbohydrate Polymers* 86.2 (2011), pp. 441–447.

[32] Matic Herman, Marko Jankovec, and Marko Topic. “Optimal I-V Curve Scan Time of Solar Cells and Modules in Light of Irradiance Level.” In: *International Journal of Photoenergy* (2012), p. 11. DOI: 10.1155/2012/151452. URL: http://dx.doi.org/10.1155/2012/151452.

[33] Michele Giulianini et al. “Current-voltage characteristics of poly(3-hexylthiophene) diodes at room temperature.” In: *Applied Physics Letters* 94.8, 083302 (2009), pp. –. DOI: http://dx.doi.org/10.1063/1.3086882. URL: http://scitation.aip.org/content/aip/journal/apl/94/8/10.1063/1.3086882.

[34] Byoungnam Park, Nam-Ho You, and Elsa Reichmanis. "Exciton dissociation and charge trapping at poly(3-hexylthiophene)/phenyl-C61-butyric acid methyl ester bulk heterojunction interfaces: Photo-induced threshold voltage shifts in organic field-effect transistors and solar cells." In: *Journal of Applied Physics* 111.8, 084908 (2012), pp. –. DOI: http://dx.doi.org/10.1063/1.4705277. URL: http://scitation.aip.org/content/aip/journal/jap/111/8/10.1063/1.4705277.

[35] L. J. A. Koster et al. "Light intensity dependence of open-circuit voltage of polymer:fullerene solar cells." In: *Applied Physics Letters* 86.12, 123509 (2005), pp. –. DOI: http://dx.doi.org/10.1063/1.1889240. URL: http://scitation.aip.org/content/aip/journal/apl/86/12/10.1063/1.1889240.

[36] Wolfgang Tress and Olle Inganäs. "Simple experimental test to distinguish extraction and injection barriers at the electrodes of (organic) solar cells with S-shaped current–voltage characteristics." In: *Solar Energy Materials and Solar Cells* 117.0 (2013). Dye Sensitized Solar Cells, Organic, Hybrid Solar Cells and New Concepts Dye Sensitized Solar Cells, Organic, Hybrid Solar Cells and New Concepts, pp. 599 –603. ISSN: 0927-0248. DOI: http://dx.doi.org/10.1016/j.solmat.2013.07.014. URL: http://www.sciencedirect.com/science/article/pii/S0927024813003607.

[37] A.J. Moulé and K. Meerholz. "Intensity-dependent photocurrent generation at the anode in bulk-heterojunction solar cells." English. In: *Applied Physics B* 92.2 (2008), pp. 209–218. ISSN: 0946-2171. DOI: 10.1007/s00340-008-3081-8. URL: http://dx.doi.org/10.1007/s00340-008-3081-8.

List of Figures

List of Tables

A. Material specification sheets

SIGMA-ALDRICH®

sigma-aldrich.com

3050 Spruce Street, Saint Louis, MO 63103, USA
Website: www.sigmaaldrich.com
Email USA: techserv@sial.com
Outside USA: eurtechserv@sial.com

Product Specification

Product Name:
Graphene oxide – 2 mg/mL, dispersion in H_2O

Product Number: **763705**

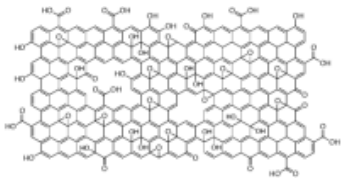

TEST	Specification
Appearance (Color)	Brown to Very Dark Brown and Black
Appearance (Form)	Liquid
Infrared spectrum	Conforms to Structure
Carbon (Dry Basis)	42.0 - 52.0 %
Sulfur (Dry Basis)	≤ 3.0 %
Potassium (K)	≤ 60 ppm
Manganese (Mn)	≤ 60 ppm
pH	
Specification: Report Only	
Mass Balance	1.9 - 2.4
mg/ml	

Specification: PRD.2.ZQ5.10000030262

SIGMA-ALDRICH®

sigma-aldrich.com

3050 Spruce Street, Saint Louis, MO 63103, USA
Website: www.sigmaaldrich.com
Email USA: techserv@sial.com
Outside USA: eurtechserv@sial.com

Product Specification

Product Name:
(+)-Sodium L-ascorbate - crystalline, ≥98%

Product Number:	**A7631**
CAS Number:	134-03-2
MDL:	MFCD00082340
Formula:	C6H7NaO6
Formula Weight:	198.11 g/mol

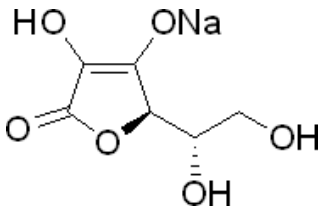

TEST	Specification
Appearance (Color)	White to Off-White
Appearance (Form)	Powder
Solubility (Color)	Colorless to Light Yellow
Solubility (Turbidity) 50 mg/ml, H2O	Clear
Infrared spectrum	Conforms to Structure
Sodium (Na)	10.8 - 12.8 %
Specific Rotation C = 1 in CO2 free H2O at 25 deg. C	103 - 108 °
Purity (TLC)	≥ 98 %
Titration with Iodine	≥ 98 %
Recommended Retest Period 5 years	----------

Specification: PRD.1.ZQ5.10000016408

SIGMA-ALDRICH®

sigma-aldrich.com

3050 Spruce Street, Saint Louis, MO 63103, USA
Website: www.sigmaaldrich.com
Email USA: techserv@sial.com
Outside USA: eurtechserv@sial.com

Product Specification

Product Name:
Silver nanowires - diam. × L 115 nm × 20–50 µm, 0.5% (isopropyl alcohol suspension)

Product Number: **739448**
CAS Number: 7440-22-4

Formula: Ag
Formula Weight: 107.87 g/mol

Ag

TEST	Specification
Appearance (Color)	Grey
Appearance (Form)	Suspension
Proton NMR spectrum	Conforms to Structure
ICP Major Analysis	Confirmed
Confirms Silver Component	
Length	Confirmed
20-50um	
Diameter	Confirmed
115 nm + /-15 nm	
Concentration	Confirmed
0.5 wt.% in IPA	

Specification: PRD.0.ZQ5.10000044099

SIGMA-ALDRICH®

sigma-aldrich.com

3050 Spruce Street, Saint Louis, MO 63103, USA
Website: www.sigmaaldrich.com
Email USA: techserv@sial.com
Outside USA: eurtechserv@sial.com

Product Specification

Product Name:
Poly(3,4-ethylenedioxythiophene)-poly(styrenesulfonate) - 1.1% in H_2O, neutral pH, high-conductivity grade

Product Number: **739324**

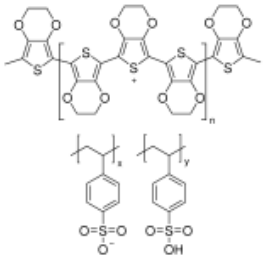

TEST	Specification
Appearance (Color)	Dark Blue to Very Dark Blue
Appearance (Form)	Liquid
Proton NMR spectrum	Conforms to Structure
pH	6.0 - 8.0
Viscosity	≤ 70 cps
Temperature	
Temperature (viscosity), Deg C	
Solid Content	1.0 - 1.2 %
Miscellaneous Assay	≤ 100
Resistivity, Ohm/sq	
Note	Note
Product of Agfa-Gevaert N.V.	

Specification: PRD.1.ZQ5.10000034896